Effect of tributary inflow on reservoir turbidity current

Authors' information is deleted for blind peer-review.

ABSTRACT

Fluvial flows carrying high sediment loads may plunge into reservoirs to form turbidity currents. However, the effects of tributary inflows on reservoir turbidity currents have remained poorly understood to date. Here a 2D double layer-averaged model is used to investigate a series of laboratory-scale numerical cases. By probing into the hydro-sediment-morphodynamic processes, we find that tributary location and inflow conditions have distinct effects on the formation and propagation of reservoir turbidity currents, and lead to complicated flow dynamics and bed deformation at the confluence. Two flow exchange patterns are generated at the confluence: turbidity current intrusion from the main channel into the tributary; and highly concentrated, sediment-laden flow plunging from the tributary into the turbidity current in the main channel. Tributary sediment-laden inflow may cause the stable plunge point to migrate downstream and is conducive to propagation of the turbidity current, whilst the opposite holds in the case of clear-water inflow from the tributary. Tributary inflow leads to a lower sediment flushing efficiency as compared to its counterpart without a tributary. Yet a high sediment concentration in the tributary may reinforce turbidity current in the reservoir, thereby increasing sediment flushing efficiency. Around the confluence, the planar distributions of velocity and bed shear stress of the turbidity current resemble their counterparts in confluence flows carrying low sediment loads or clear water. Yet, the bed exhibits aggradation near the confluence due to the turbidity current, in contrast to pure scour in a river confluence with a low sediment load. Appropriate account of tributary effects is required in studies of reservoir turbidity currents, and for devising strategies for long-term maintenance of reservoir capacity.

KEYWORDS

reservoir; turbidity current; tributary; sediment flushing efficiency; double layer-averaged model

Highlights

- Tributary inflow may cause the stable plunge point of reservoir turbidity current to migrate either upstream or downstream and modify its propagation.
- Tributary inflow may lead to lower sediment flushing efficiency by reservoir turbidity current.
- Tributary discharge and sediment concentration may lead to disparate bed deformation at confluence.

1 Introduction

Heavily sediment-laden rivers usually involve: flows whose fluid properties have non-Newtonian rheology [1, 2], rapid bed evolution such as bed-tearing scour [3], river blockage [4, 5], active main channel-floodplain interactions leading to disparate morphological patterns in main channels and over floodplains [6], and increased peak discharge along the river [7, 8]. To generate electricity, prevent floods, supply water, and provide irrigation capacity, many large reservoirs have been built on rivers, some of which carry high sediment loads. The hydrological and morphological impacts of large reservoirs can be dramatic, as exemplified by the Yellow River — a river featuring the highest sediment flux in the world [9]. Rivers with high sediment loads, such as the Yellow River and its tributaries in the Loess Plateau, China, often feature extremely complicated flow-sediment-bed interactions. Under certain conditions, subaerial sediment-laden flows in reservoirs may plunge to form turbidity currents as subaqueous sediment-laden flows. Theoretically, turbidity currents exhibit complicated fluid-particle interactions whose mechanisms are not yet fully understood [10, 11]. In practice, turbidity currents are highly desirable for flushing sediment as much as possible out of reservoirs, thereby alleviating sedimentation and capacity loss [12]. Moreover, the venting effect of turbidity currents acts as an ecological favour to the downstream environment by transporting fine sediment [13], if attention is paid to limit the environmental impacts of the turbidity increase.

Over recent decades, many investigations have been undertaken on reservoir turbidity currents [12, 14-17]. Computational modeling has become widely used to resolve the detailed processes of reservoir turbidity currents. Full 3D models (e.g., [18, 19]) are not presently feasible for resolving large-scale turbidity currents, even though they have greater theoretical rigour than 1D and 2D models. As a compromise between computational expense and theoretical accuracy, a coupled 2D layer-averaged model was proposed to resolve turbidity currents in the Xiaolangdi reservoir in the Yellow River [15]. Lai et al. [20] developed a 2D layer-averaged model for turbidity currents that matched results from physical model tests of Shihmen Reservoir, Taiwan. Based on an empirical plunge criterion, Wang et al. [16, 21] proposed a one-dimensional model for open channel flows and turbidity currents while ignoring differences between incipient and stable plunge criteria that have since been revealed by theoretical analysis [22, 23] and flume experiments [24]. Critically, these models can only resolve the propagation of turbidity currents after their formation, and do not reflect the impact of reservoir operation on their formation and propagation. As the present state-of-the-art, the coupled 2D double layer-averaged model proposed by Cao et al. [12] is capable of resolving the whole series of processes behind reservoir turbidity currents, from formation and propagation to recession. This model, along with its recent extended version, has recently been applied to resolve landslide-generated waves, and barrier lake formation and breach processes [25-27].

Flow exchange between the main channel (MC) and tributary (TR) can occur either as open channel flow or as a turbidity current in the TR, both of which significantly impact on the evolution of a turbidity current in the MC. Studies have examined the turbidity current in the main river as clear-water flow enters from a TR [16, 21, 28-30]. Intrusion of the turbidity current from the MC to a TR is an essential factor in reducing the discharge and sediment concentration of the current [31], which also advances the location and formation of the plunge point, decelerates the turbidity current, and promotes bed aggradation, causing the sediment flushing efficiency to become relatively small [28]. Several physical experiments have focused on open channel flow in a main river with hyperconcentrated tributary flows [32, 33]. Such conditions lead to increased sediment deposition and more noticeable bars at the confluence than for one experiencing ordinary sediment-laden flow. Nevertheless, previous studies have been mostly limited to turbidity currents arising solely from the MC or a TR. Physically, sediment-laden flows carrying high sediment loads from both the MC and a TR have different characteristics compared to a confluence carrying an ordinary sediment load. In short, the understanding as to how reservoir turbidity currents are modified by tributary inflows is presently far from clear.

This paper sets out to unravel the impact of tributary inflow (in terms of discharge, sediment concentration, and junction location) on a reservoir turbidity current in the MC. A coupled 2D double layer-averaged model proposed by Cao et al. [12] is used to investigate a series of laboratory-scale numerical cases. By probing into the computational results, we aim to shed light on the effect of a TR on the formation and propagation of reservoir turbidity currents, and the flow dynamics of turbidity currents near a confluence.

2 Methods

A series of laboratory-scale numerical cases are designed on the basis of flume experiments on reservoir turbidity currents by Lee and Yu [24], along with presumed tributary settings and inflows (Fig. 1). A 2D double layer-averaged SHSM model [12] is applied to resolve the flow and sediment transport processes. Based on the numerical results, the impacts of tributary inflow on reservoir turbidity current are evaluated. The methods are briefly described as follows.

2.1 2D hydro-sediment-morphodynamic model

The 2D double layer-averaged model proposed by Cao et al. [12] has been benchmarked against a series of experimental turbidity currents related to lock-exchange [34] and sustained inflows [24], and also successfully applied to the whole process of turbidity currents in the Xiaolangdi Reservoir in the middle Yellow River, China. The model has been further extended to investigate wave and sediment transport processes due to landslides impacting reservoirs [24] as well as barrier lake formation and breach processes [25]. This model is applied in the present study, as outlined below.

The governing equations are derived from the fundamental conservation laws in fluid dynamics under the framework of shallow water hydrodynamics, including mass and momentum conservation equations for the upper clear-water flow layer and the lower sediment-laden flow layer (e.g., turbidity current), the mass conservation equation for sediment carried by the turbidity current, and the mass conservation equation for bed sediment. For the upper layer, ρ_w is the density of water, h_w denotes thickness, u_w and v_w are the layer-averaged velocity components in the *x*- and *y*-directions. For the lower layer,

ρ_s is the density of sediment, $\rho_c = \rho_w(1-c_s)+\rho_s c_s$ is the density of the water-sediment mixture, h_s denotes thickness, u_s and v_s are the layer-averaged velocity components in the *x*- and *y*-directions, and c_s is the total volumetric sediment concentration. Bed elevation is denoted by z_b.

A set of relationships is introduced to determine the bed resistance and interface shear stress, water entrainment E_w, and net sediment exchange flux (i.e., entrainment E minus deposition D). Specifically, Manning's formula is used to calculate bed shear stresses. Shear stresses at the interface between the upper and lower layers are estimated in a similar fashion. Water entrainment at the interface is calculated using the Richardson number, following Parker et al. [35]. Sediment deposition is determined using the sediment particle settling velocity and near-bed concentration. Bed entrainment flux is estimated using Zhang and Xie's formula for suspended sediment transport capacity [36].

The governing equations of the model proposed by Cao et al. [12] are synchronously solved as two hyperbolic systems, one for the upper layer, the other for the lower layer. Each hyperbolic system is solved by a quasi-well-balanced numerical algorithm involving drying and wetting, using an accurate finite volume Godunov-type approach in conjunction with the HLLC (Harten-Lax-van Leer Contact Wave) approximate Riemann solver on a fixed rectangular mesh. The present numerical scheme is explicit, and so the time step is controlled by the Courant-Friedrichs-Lewy condition.

2.2 Test cases

A series of laboratory-scale numerical cases are designed to complement the flume experiments by Lee and Yu [24]. As the experiments originally did not involve a tributary (TR), a hypothetical TR is herewith set to the right-hand side of the main channel (MC), with the TR meeting the MC at a junction angle θ of 90^o or 45^o. Two junction locations are considered, and the distance L_t from dam to junction equals 10 m or 15 m. The MC dimensions are $20\times0.2\times0.6\,\text{m}$, and its bottom slope is $i_{bm}=0.02$. The hypothetical TR is rectangular and 17 m long by 0.30 m deep, with 0.1 m or 0.2 m width. The TR-to-MC width ratio is defined by $W_r=W_t/W_m$, where W_t and W_m are the widths of TR and MC. The bed slope of the TR can also be adjusted, and two values of bed slope, $i_{bt}=0.012, 0.02$, are considered (Fig. 1). In the experiments of Lee and Yu [27], there was no bottom outlet for sediment flushing at the downstream end of the flume. Herein a dam is located at the downstream end of the flume, and a bottom sediment flushing tunnel (BSFT) controlled by a bottom sluice gate, 4 cm high, is set for sediment flushing, following Cao et al. [12].

Based on combinations of different inflows from the MC and TR, three series of numerical cases are designed as summarized in Table 1, i.e., Series A for sediment-laden flow from the MC without a TR; Series B for sediment-laden flow from the MC with clear-water flow from the TR; Series C for sediment-laden flows from both the MC and TR. The cases enable the effects of TR-to-MC discharge ratio and sediment concentration ratio to be identified. The TR-to-MC discharge ratio is defined by $Q_r=Q_t/Q_m$, where Q_t and Q_m are discharges of TR and MC. The TR-to-MC sediment concentration ratio is defined by

$C_r = C_t / C_m$, where C_t and C_m are the volumetric sediment concentrations of TR and MC. The inflow discharge Q_m is $0.001358\,\mathrm{m^3/s}$, and the volumetric sediment concentration C_m is 0.05 or 0.00667. More controls upon the effects of tributary inflow on reservoir turbidity current are considered as the junction angle θ, the width ratio W_r and the bed slope i_{bt} of the TR. Table 2 summarizes the tributary configuration and inflow conditions for Series A, B and C.

The present computations presume initially steady, gradually varied, clear-water flow in accordance with the prescribed discharges in the MC and TR, and an undisturbed water depth h_0 of 0.34 m immediately upstream of the dam.

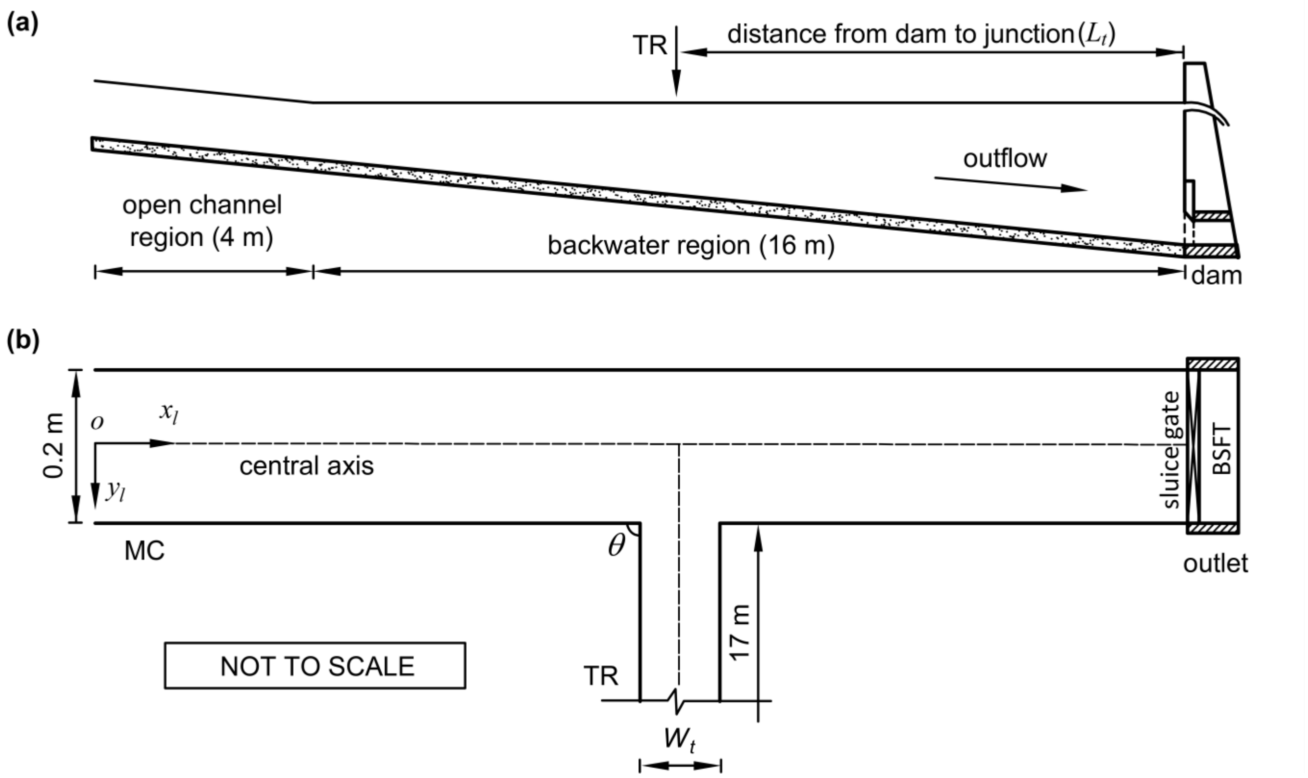

Fig. 1 Vertical profile **(a)** and plan view **(b)** of the main channel (MC) and tributary (TR)

At the inlet cross-section in the MC, the prescribed discharge and sediment concentration (Table 2) determine the boundary conditions for the subaerial sediment-laden flow layer, when there is no clear-water flow layer. At the inlet cross-section in the TR, if the inflow contains sediment, the boundary conditions are specified in a similar manner as for the MC; otherwise, the prescribed discharge (Table 2) is used to specify the boundary condition for the clear-water flow, when there is no sediment-laden flow layer. The boundary conditions are implemented using the method of characteristics.

At the outlet cross-section, before the arrival of the turbidity current front at the dam, the bottom sluice gate is closed, and there is no outflow discharge of the turbidity current. The depth and velocity of the upper clear-water flow layer are determined by the method of characteristics according to the outflow discharge, Q_{wo} , which is set to be equal to the sum of inflow discharges from the MC and TR. Upon arrival of the turbidity current front at the dam, the clear-water outflow of the upper layer is halted, and the bottom sluice gate simultaneously opened, with the outflow discharge estimated from the following empirical formula for sluice gate outflow,

$$Q_{so} = \mu b e \sqrt{2g' H_0} \tag{1}$$

where H_0 is the hydraulic head of the turbidity current, approximated by its elevation H ; $\mu = 0.60\text{-}0.18 e/H$ is the discharge coefficient; $g' = sgc_s$ is the submerged gravitational acceleration; and $s = (\rho_s/\rho_w) - 1$ is the specific gravity of sediment; the bottom sluice gate height e is set to 4 cm; and the bottom sluice gate width b is set to 20 cm.

The bed roughness Manning coefficient is $n_b = 0.015\,\mathrm{m}^{-1/3}\mathrm{s}$, and the interface roughness Manning coefficient is $n_i = 0.005\,\mathrm{m}^{-1/3}\mathrm{s}$, following Cao et al. [12]. The suspended material is kaolin having a specific gravity of 2.65 and a mean particle size of 6.8 μm. In the computational model, the converged spatial steps are 0.025 m in both longitudinal and lateral directions.

Table 1. Arrangement of computational cases

Series	ID number	Context
A	A1-A2	Sediment-laden flow from MC without TR
B	B1-B12	Sediment-laden flow from MC with clear-water flow from TR
C	C1-C14	Sediment-laden flows from both MC and TR

Table 2. Summary of tributary configuration and inflow conditions

Series	Distance from dam to junction		Inflow conditions			Tributary configuration		
	$L_t = 15\mathrm{m}$	$L_t = 10\mathrm{m}$	C_m	Q_r	C_r	W_r	i_{bt}	θ
A	A1		0.05	/	/	/	/	/
	A2		0.00667					
B	B1	B2	0.05	0.736	0.0	0.5	0.012	90°
	B3	B4		1.473				
	B5	B6	0.00667	0.736				
	B7	B8	0.05	1.473		1.0		
	B9	B10				0.5	0.02	
	B11	B12					0.012	45°

<table>
<tr><td rowspan="7">C</td><td>C1</td><td>C2</td><td rowspan="3">0.05</td><td>0.736</td><td>1.334</td><td rowspan="4">0.5</td><td rowspan="5">0.012</td><td rowspan="6">90°</td></tr>
<tr><td>C3</td><td>C4</td><td rowspan="2">1.473</td><td>0.667</td></tr>
<tr><td>C5</td><td>C6</td><td rowspan="5">1.334</td></tr>
<tr><td>C7</td><td>C8</td><td>0.00667</td><td>0.736</td></tr>
<tr><td>C9</td><td>C10</td><td rowspan="3">0.05</td><td rowspan="3">1.473</td><td>1.0</td></tr>
<tr><td>C11</td><td>C12</td><td rowspan="2">0.5</td><td>0.02</td></tr>
<tr><td>C13</td><td>C14</td><td>0.012</td><td>45°</td></tr>
</table>

3 Results and discussion

3.1 Characteristics at the plunge point

Here we evaluate the effects of tributary inflow and sediment inputs on the formation of MC turbidity currents based on the numerical results (Cases A1, B1-B4, C1-C6 in Table 2). The transition from subaerial open channel sediment-laden flow to subaqueous turbid flow features reservoir turbidity current formation, with unstable plunge points that initially move forward. By t ~ 100 s, the plunge points have stabilized in Cases A1, B1-B4 and C1-C6, and the turbidity current fronts have not yet arrived at the bottom outlet.

Fig. 2 shows a definition sketch of the stable plunge region along the central line of MC, where x_{ps} is the distance between the stable plunge point and main flume entrance; h_{ps} is the turbidity current thickness at the stable plunge point; E_w is the mass flux of water entrainment across the interface between the two layers; and E, D are the sediment entrainment and deposition fluxes. Table 3 lists the location x_{ps}, depth h_{ps}, and densimetric Froude number $F_{ps} = u_s / \sqrt{sgc_s h_{ps}}$ at stable plunge points along the central line of the MC, corresponding to the different inflow conditions and junction locations considered (Cases A1, B1-B4, C1-C6 in Table 2). Fig. 3a displays the locations of stable plunge points in the MC. Later, in all cases by $t > 120\,\text{s}$, the turbidity currents become able to flush sediment through the BSFT, and the plunge point gradually changes location, as indicated in Fig. 3b at t = 2 h.

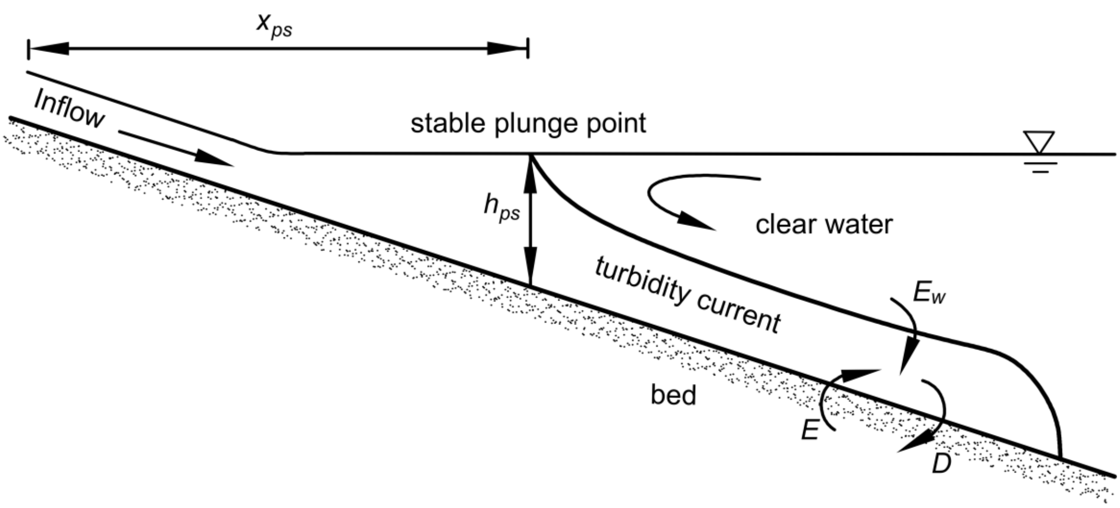

Fig. 2 Definition sketch of reservoir flow featuring turbidity current

Table 3 Parameters of stable plunge points along the central line of MC at t = 100 s

Q_r	C_r	$L_t = 15\text{m}$				$L_t = 10\text{m}$			
		Case	x_{ps} (m)	h_{ps} (cm)	F_{ps}	Case	x_{ps} (m)	h_{ps} (cm)	F_{ps}
/	/	A1	5.375	4.74	0.67	—	—	—	—
0.736	0.0	B1	4.95	4.80	0.67	B2	5.35	4.78	0.66
	1.334	C1	6.20	6.07	0.75	C2	5.55	4.81	0.65
1.473	0.0	B3	4.875	4.65	0.68	B4	5.275	4.77	0.66
	0.667	C3	7.60	8.86	0.77	C4	5.575	4.87	0.67
	1.334	C5	6.80	7.45	0.76	C6	5.55	4.86	0.66

Table 3 and Fig. 3a present flow parameters at the stable plunge point at t = 100 s for

Cases A1, B1-B4 and C1-C6. For convenience, we define the stable plunge point of reservoir turbidity current in the case without a TR as the original stable plunge point (OSPP). For Cases A1, B1-B4 and C1-C6, OSPP locates at $x_l = 5.375\,\mathrm{m}$. Clear-water flow from the TR causes the stable plunge point to migrate upstream of the OSPP, as demonstrated in Cases B1-B4. However, heavily sediment-laden inflow from the TR increases the discharge and sediment concentration of the MC turbidity current, causing its stable plunge point to migrate downstream of the OSPP. After 2 hrs, the plunge point in Series C cases migrates further downstream, characterizing the feedback effect of significant bed deformation (subsection 3.6), whereas the plunge point position in the other Series A and Series B cases hardly changes with time (Fig. 3b).

Tributary inflow conditions and junction location lead to distinct effects on the plunge point of the turbidity current in the MC. We consider two different distances from dam to junction, L_t = 15 m and 10 m, one of which is located upstream and the other downstream of the OSPP. In Series B, the stable plunge point is located further upstream for the larger discharge ratio, and this effect is most pronounced when the junction is located upstream of the OSPP (Case B3). In Series C, if the junction is located upstream of the OSPP, then x_{ps}, h_{ps}, and F_{ps} along the central line tend to increase as the tributary inflow discharge increases, but decrease as the tributary sediment concentration increases (Table 3). This occurs primarily because either larger discharge or smaller sediment concentration of the lower sediment-laden flow layer (e.g., turbidity current) promotes further water entrainment. Furthermore, for $C_r > 1$, the stable plunge point in the MC moves downstream (Cases C1 and C5). For $C_r < 1$, the stable plunge point near the TR migrates downstream (Case C3). For a finite value of sediment concentration ratio, there is a lateral variation in plunge point position. By contrast, if the junction is located downstream of the OSPP, the effect of tributary inflow on turbidity current formation is minor (Cases C2, C4 and C6).

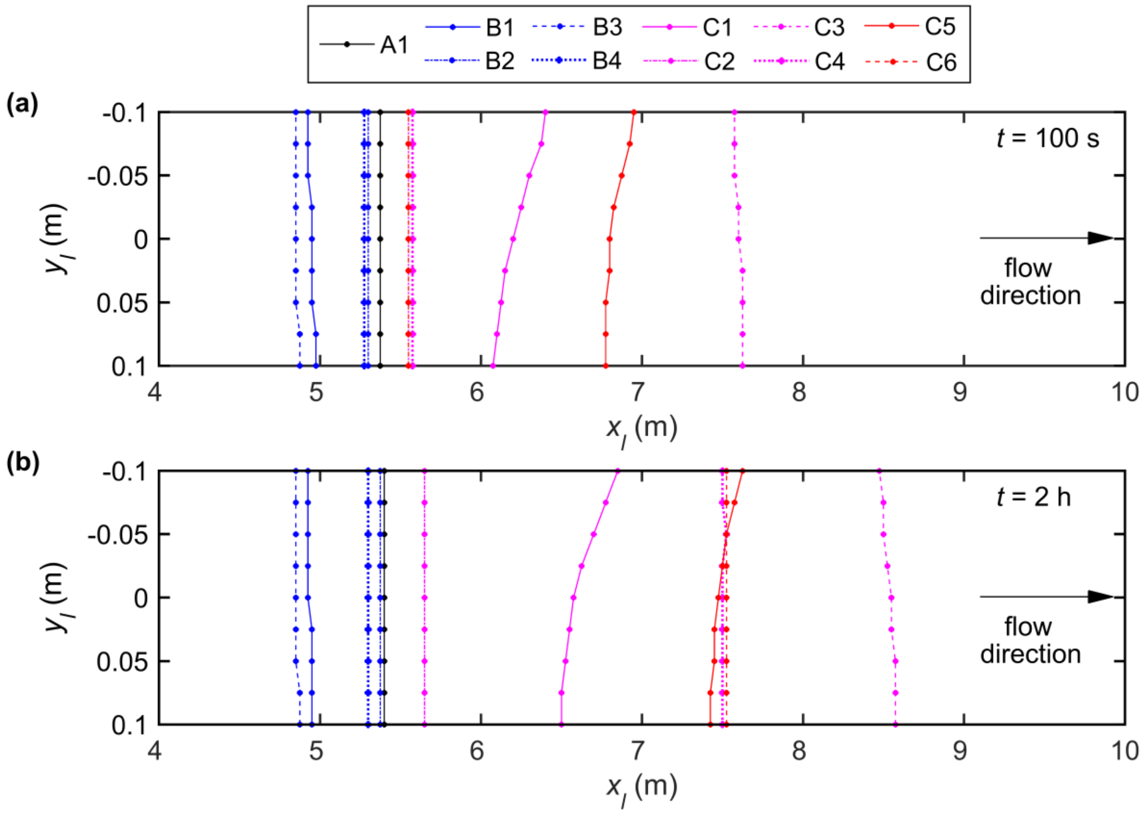

Fig. 3 Turbidity current plunge point locations in the MC at **(a)** $t = 100\,\mathrm{s}$, **(b)** $t = 2\,\mathrm{h}$ for Cases A1, B1-B4, and C1-C6 listed in Tables 2 and 3

3.2 Advance of turbidity current front

Fig. 4 illustrates the front locations of the MC turbidity currents for Cases A1, B1-B4, C1-C6 in Table 2. Hardly any difference is discernible in the front location moving along three lines across the MC at $y_l = -0.05\,\mathrm{m}, 0\,\mathrm{m},$ and $0.05\,\mathrm{m}$, indicating that the tributary inflow conditions have little effect on the advance of turbidity currents in the lateral direction. In the longitudinal direction, clear-water flow from the TR slows down the propagation of turbidity current, as in the Series B cases. It should be emphasized that the boundary inflows of the MC and TR in Series C are sediment-laden compared to the initial clear-water flows. Therefore, before interacting with the upstream sediment-laden flow entering from the TR, the turbidity current of Series C propagates more slowly than that of Series A. By contrast, the turbidity current of Series C advances faster at a larger discharge ratio as the heavily sediment-laden flow from the TR plunges into the MC turbidity current (Cases C3-C6).

Compared to Case A1 without a TR, the MC turbidity current propagation is slower for a larger discharge ratio in Series B (Cases B1 and B3, B2 and B4). Physically, clear-water flow from the TR dilutes the MC turbidity current, while the MC turbidity current simultaneously intrudes into the TR. Both phenomena cause the sediment concentration of the MC turbidity current to reduce, thus reducing the gravity difference between the MC turbidity current and ambient fluid (clear water). Consequently, the MC turbidity current propagates more slowly than in a corresponding case without a TR. By contrast, the larger the discharge of sediment-laden flow from the TR, the faster the turbidity current propagates (Cases C1 and C5, C2 and C6). Furthermore, the higher the sediment concentration (corresponding to a larger driving force) of sediment-laden flow from the TR, the faster the MC turbidity current propagates, as evidenced by Cases C3 and C5, C4 and C6. Tributary effects on the propagation of turbidity current are most evident when the junction is located upstream of the OSPP (Cases C3 and C5).

The results are further extended for other values of L_{st} (distance from the junction location to OSPP), corresponding to Fig. S1 shown in the Supporting Information online. Fig. S1 displays the time history of turbidity current front location at the central line ($y_l = 0\,\mathrm{m}$) of the MC for Cases A2, B5-B6, and C7-C8. It should be noted that the stable plunge point of Case A2 with lower volumetric sediment concentration locates further downstream than that of Case A1. Succinctly, tributary inflow conditions have a discernible effect on front location, and so warrant appropriate treatment in reservoir sediment management schemes.

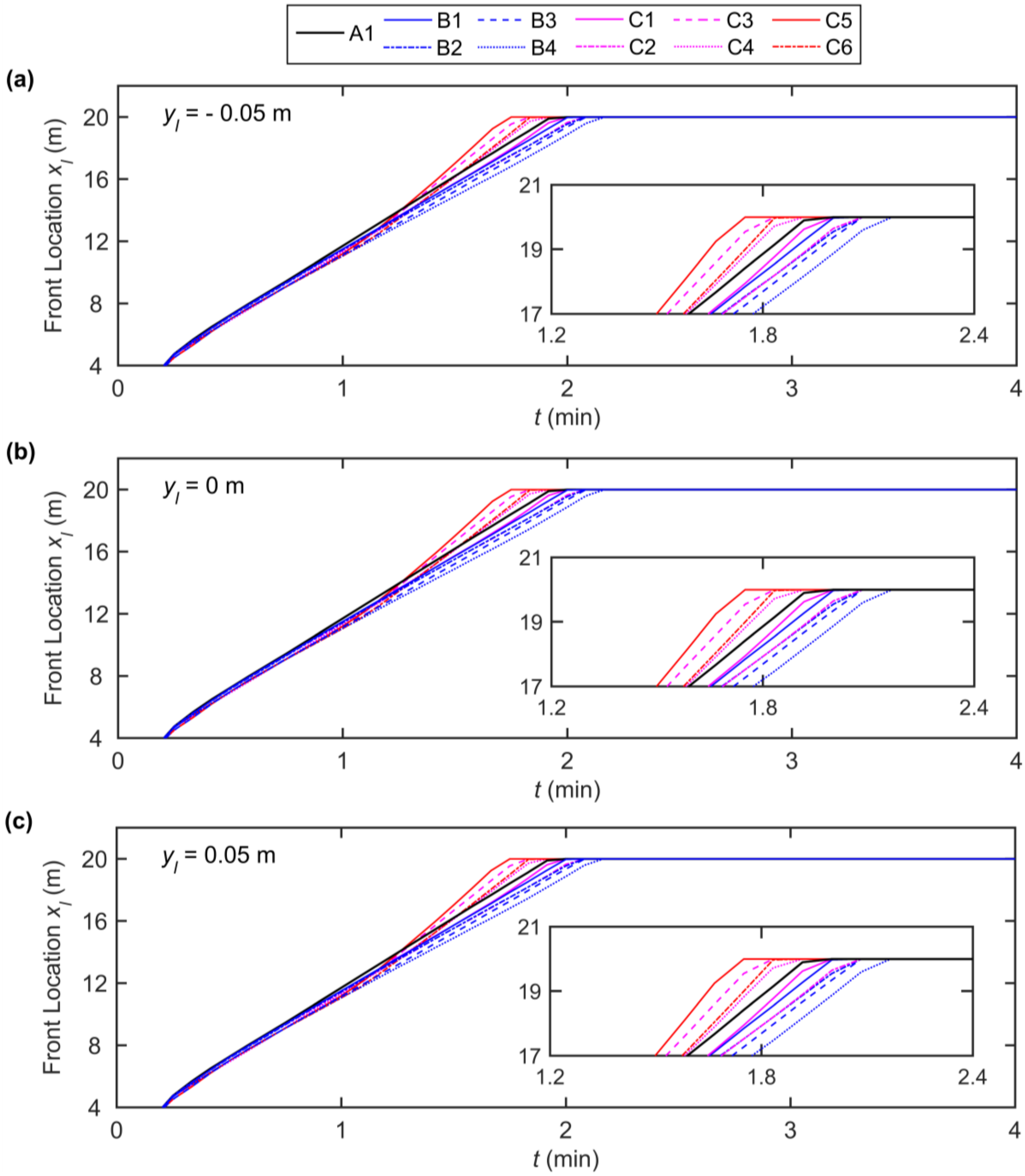

Fig. 4 Time history of turbidity current front at three transverse locations across the MC: **(a)** $y_l = -0.05\,\mathrm{m}$; **(b)** $y_l = 0\,\mathrm{m}$; **(c)** $y_l = 0.05\,\mathrm{m}$ for Cases A1, B1-B4, and C1-C6 listed in Tables 2 and 3

3.3 Turbidity current thickness

We now delve into the effect of tributary inflow on turbidity current thickness. Fig. 5 displays planar distributions of turbidity current thickness for Case A1 without a TR at three time instants ($t = 60\,\mathrm{s}$, $240\,\mathrm{s}$, $2\mathrm{h}$) and for Cases B1, C1, C3, and C5 when the junction is located upstream of the OSPP. Fig. 6 shows the planar distributions of turbidity current thickness for Cases B2, C2, C4, and C6 when the junction is located downstream of the OSPP.

By $t = 60\,\mathrm{s}$, the subaerial sediment-laden flow in the MC for the Series B and C cases has turned into a turbidity current and intruded from the MC to TR, and so its thickness at the junction is smaller than for Case A1 without a TR (Figs. 5a and 6a). By $t = 240\,\mathrm{s}$, the turbidity current fronts in all cases have reached the dam (Fig. 4). In Series C, sediment-laden flow from the TR encounters the MC turbidity current, whose thickness increases at the junction owing to the discharge of water and sediment from the TR (Figs. 5b and 6b). Moreover, in series C, a larger turbidity current thickness is generally obtained with a larger discharge ratio and a lower sediment concentration ratio, as evident in Cases C3 and C5. In Cases B1 and B2 at $t = 2\,\mathrm{h}$, the MC turbidity current continuously intrudes into the TR, and its thickness at the junction is smaller than Case A1 without a TR. By contrast, for the Series C cases, when the junction is located upstream of the OSPP, the turbidity current thickness in Cases C1 and C5 with $C_r > 1$ is smaller downstream of the junction corner, whereas the turbidity current thickness in Case C3 with $C_r < 1$ is larger without significant lateral variation (Fig. 5c), reflecting the effect of bed deformation near the confluence (subsection 3.6). When the junction is located downstream of the OSPP, the thickness at the junction for Cases C2, C4 and C6 is larger than for Case A1 (Fig. 6c).

The thickness of a turbidity current at a confluence exhibits high temporal and spatial variability. Differences in flow exchange patterns cause lateral variation in turbidity current thickness at the confluence. Reservoir turbidity current intrusion from the MC to TR leads to smaller turbidity current thickness at the junction than for Case A1 without a TR. However, highly concentrated sediment-laden flow plunging from the TR into the MC turbidity current leads to larger longitudinal thickness. This occurs primarily because sediment-laden flow from the TR induces more water and sediment into the MC turbidity current. Nevertheless, in a long-term hydro-sediment-morphodynamic process, the turbidity current thickness is affected by bed deformation and boundary conditions in the reservoir.

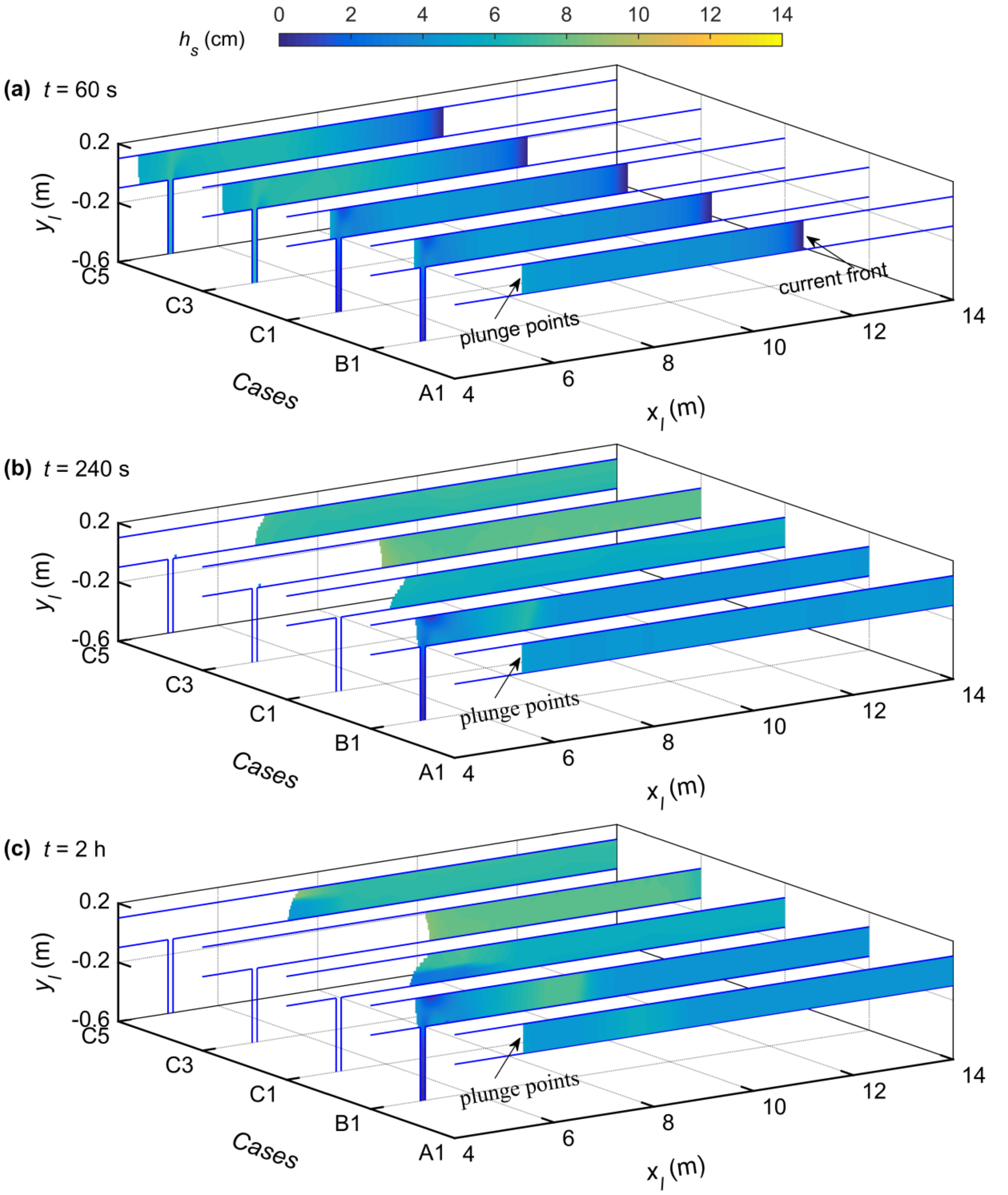

Fig. 5 Planar distributions of turbidity current thickness h_s for Cases A1, B1, C1, C3 and C5 with the junction is located upstream of the OSPP at **(a)** $t = 60\,\mathrm{s}$, **(b)** $t = 240\,\mathrm{s}$, and **(c)** $t = 2\,\mathrm{h}$

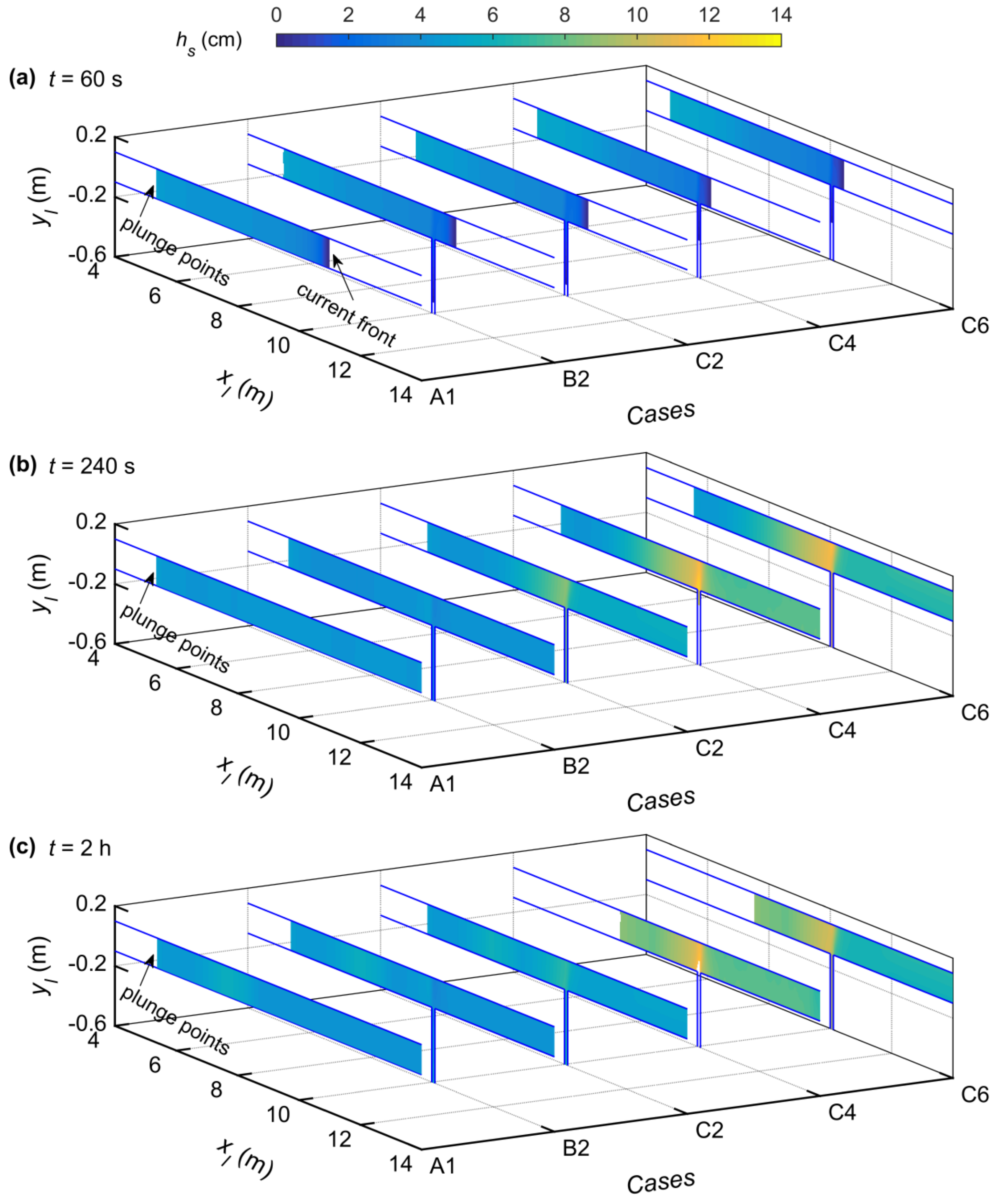

Fig. 6 Planar distributions of turbidity current thickness h_s for Cases A1, B2, C2, C4 and C6 with the junction is located downstream of the OSPP at **(a)** $t = 60\,\text{s}$, **(b)** $t = 240\,\text{s}$, and **(c)** $t = 2\,\text{h}$

3.4 Turbidity current velocity field

We now evaluate the effect of tributary inflow on the turbidity current velocity field near the confluence. For a reservoir turbidity current with distinct tributary inflow, two flow exchange patterns are generated at the confluence: the reservoir turbidity current intrudes from the MC to TR (Series B), while highly concentrated, sediment-laden flow plunges from the TR into the MC reservoir turbidity current (Series C). Although many investigations have examined open channel flow at a confluence [37-45], none has considered highly concentrated, sediment-laden flow. A previous experimental study on open channel confluences carrying low sediment loads revealed that the flow structure can be divided into six regions [40]: (i) a stagnation zone with reduced flow velocity at the upstream junction corner between the MC and TR; (ii) a deflection zone at the entry to the junction; (iii) a flow separation zone commencing at the downstream junction corner; (iv) a region of maximum velocity near the centre of the MC just downstream of the junction; (v) a flow recovery area further downstream of the junction; and (vi) shear layers between the two confluence flows.

To gain more insight into the flow dynamics of reservoir turbidity currents, we now examine the resultant layer-averaged velocity ($U_s = \sqrt{u_s^2 + v_s^2}$) of the sediment-laden flow layer and associated bed shear stress ($\tau_b = \rho_c g n_b^2 U_s^2 / h_s^{1/3}$) for Cases A1, B3, C5 and C6 at flow elapsed times t = 240 s and t = 2 h. Fig. 7 depicts the lower layer-averaged velocity field and bed shear stress distribution obtained for Case A1 in the absence of a TR. By $t = 240\,\mathrm{s}$, subaerial sediment-laden flow in the MC has plunged into the clear water at $x_l = 5.375\,\mathrm{m}$, whilst the layer-averaged velocity of sediment-laden flow and bed shear stress have decreased owing to propagation of the turbidity current (Figs. 7a1 and 7b1). At $t = 2$ h, the turbidity current velocity field has hardly altered (Fig. 7a2), with the magnitude of bed shear stress generally below 1.0 N/m^2 (Fig. 7b2).

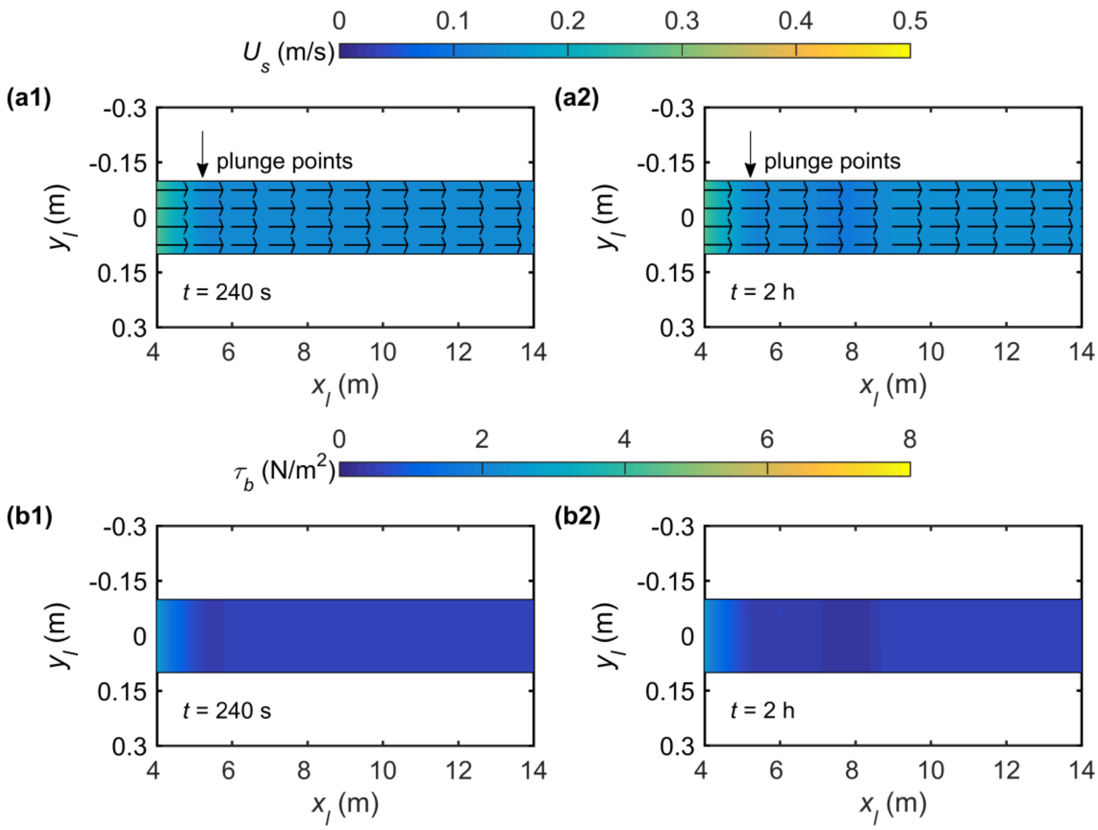

Fig. 7 **(a1-a2)** Velocity field of sediment-laden flow layer and **(b1-b2)** distribution of magnitude of bed shear stress τ_b for Case A1, at times t = 240 s and t = 2 h

Fig. 8 shows the results for Case B3 which features highly concentrated, sediment-laden flow entering the junction from the MC and clear-water flow from the TR, when the junction is located upstream of the OSPP. By t ~ 240 s, the MC turbidity current has reached the junction and intruded into the TR. The magnitude of the resultant layer-averaged velocity of the turbidity current decreases as it propagates upstream into the TR, and increases at the downstream junction corner owing to the presence of a small recirculation zone (Fig. 8a). Again at $t = 2\ \mathrm{h}$, the velocity field at the confluence hardly changes compared to that at $t = 240\,\mathrm{s}$ (Fig. 8b). The bed shear stress features are similar to that of the velocity field at the junction, with the downstream junction corner experiencing a high level of bed shear stress (Figs. 11a1 and 11a2). Therefore, there are noticeable differences in the lower-layer averaged velocity and bed shear stress distributions for Series B and Series A due to intrusion of the turbidity current from the MC to the TR (Figs. 7 and 8).

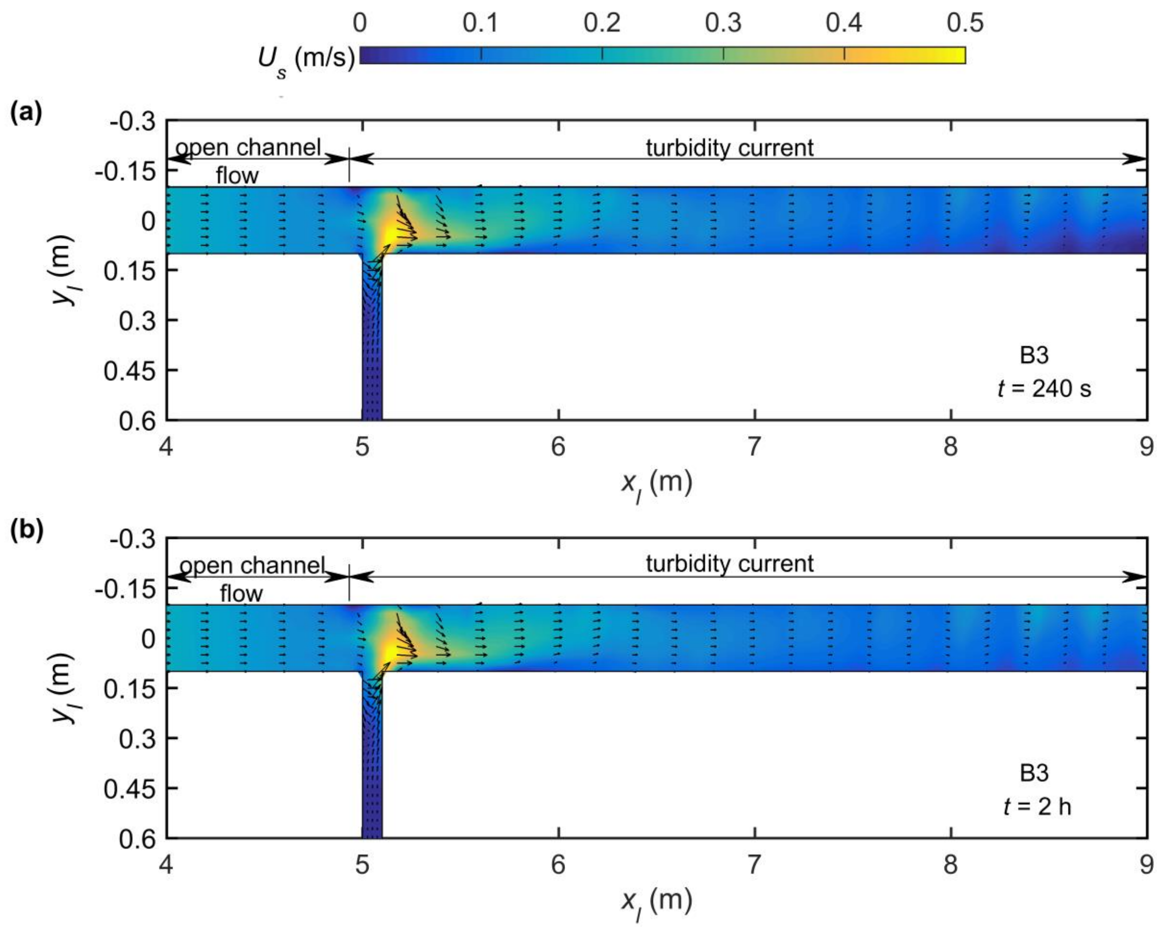

Fig. 8 Velocity field of sediment-laden flow layer for Case B3 when there is a turbidity

current within the confluence, at times **(a)** $t = 240\,\text{s}$, and **(b)** $t = 2\,\text{h}$

As shown in Fig. 9, Case C5 features highly concentrated, sediment-laden flow in both the MC and the TR at a junction located upstream of the OSPP. By $t = 240\,\text{s}$, the sediment-laden flow in the TR has encountered the turbidity current in the MC. The turbidity current plunges downstream of the junction, and the upper clear-water flow layer at the confluence disappears (Figs. 3 and 5b). At this time, the layer-averaged velocity of the sediment-laden flow at the confluence may be divided into the following zones: shear layers, a stagnation zone near the upstream junction corner, a separation zone immediately after the downstream junction corner, a deflection zone, an area of maximum velocity at the confluence, and a flow recovery zone downstream of the junction. These resemble the flow dynamic behavior at an open channel river confluence, proposed by Best [40]. The bed shear stress magnitude is directly related to the velocity field of the sediment-laden flow layer, and its value within the maximum velocity area is higher for Case C5 than for Case A1 without a TR (Figs. 7b1 and 11b1). Later, by $t = 2\,\text{h}$, the flow regions are more apparent with an enlarged separation zone, driven by the long-term hydro-sediment-morphodynamic process (Fig. 9b). Downstream of the junction, the bed shear stress is generally below 2.5 N/m^2, except in the region of maximum velocity where the bed shear stress reaches about 5 N/m^2. In Case C5, the bed shear stress values are related to the sediment-laden flow velocity in the vicinity of the confluence, and are higher than for Case A1 without a TR (Figs. 7b2 and 11b2).

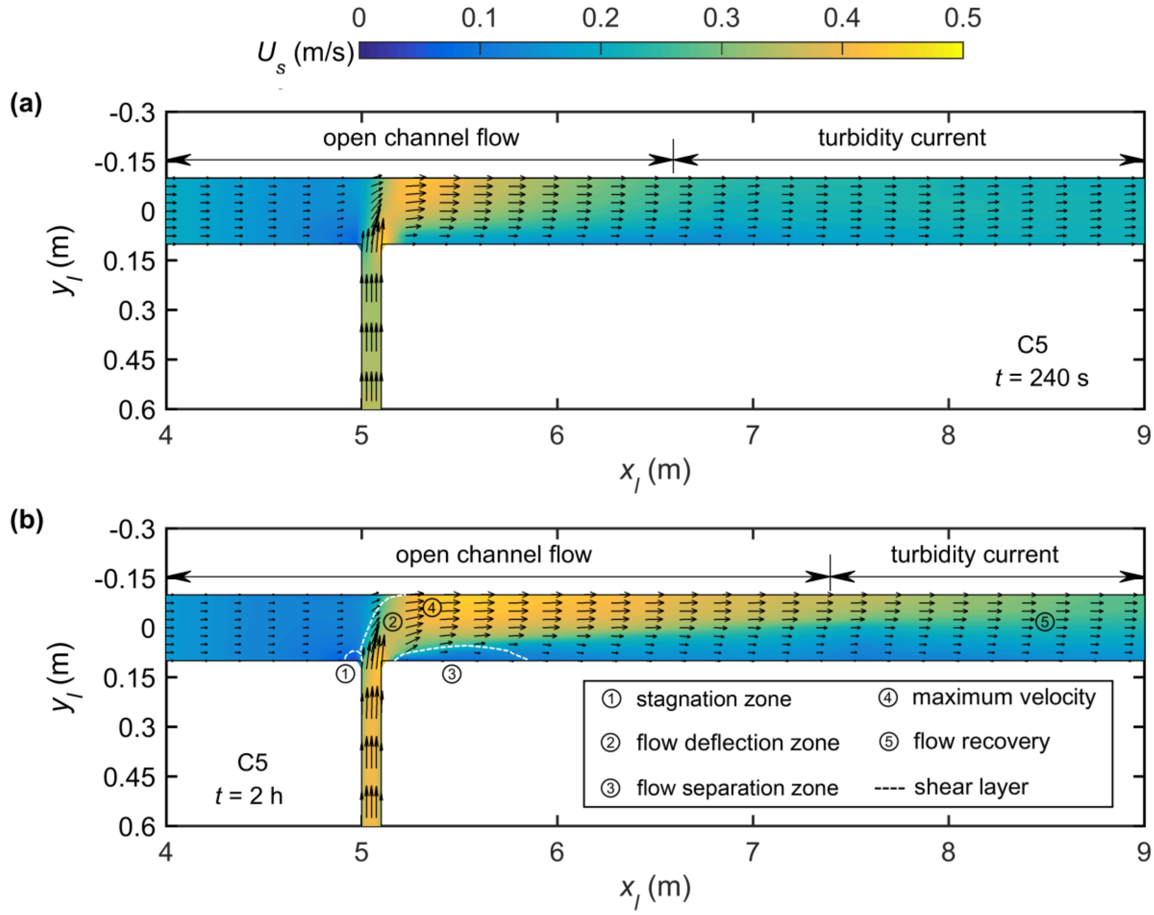

Fig. 9 Velocity field of sediment-laden flow layer for Case C5 when there is open channel flow within the confluence, at times **(a)** $t = 240\,\mathrm{s}$, and **(b)** $t = 2\,\mathrm{h}$

Fig. 10 displays the lower-layer velocity field obtained for Case C6 which features upstream highly concentrated sediment-laden flow in both the MC and the TR. In this case, the junction is located downstream of the OSPP. By $t = 240\,\mathrm{s}$, the heavily sediment-laden flow from upstream in the TR has interacted with the MC turbidity current. The velocity field of the turbidity current reveals a stagnation zone near the upstream junction corner, a deflection zone, and a maximum velocity area at the confluence (Fig. 10a). Notably, flow separation cannot be discerned, although the minimum velocity around the downstream junction corner essentially vanishes. Compared with Case C5, the size of the separation zone is greatly affected by the junction location. The bed shear stress is minimized in the stagnation zone upstream of the junction, and reaches its highest level in the region of maximum velocity downstream of the junction (Fig. 11c1). Between t = 240 s and t = 2 h, the flow pattern and bed shear stress remain stable at the confluence (Fig. 10b). The bed shear stress downstream of the junction for Case C6 is approximately equal to 2.5 N/m^2, higher than for Case A1 without a TR (Figs. 7b2 and 11c2).

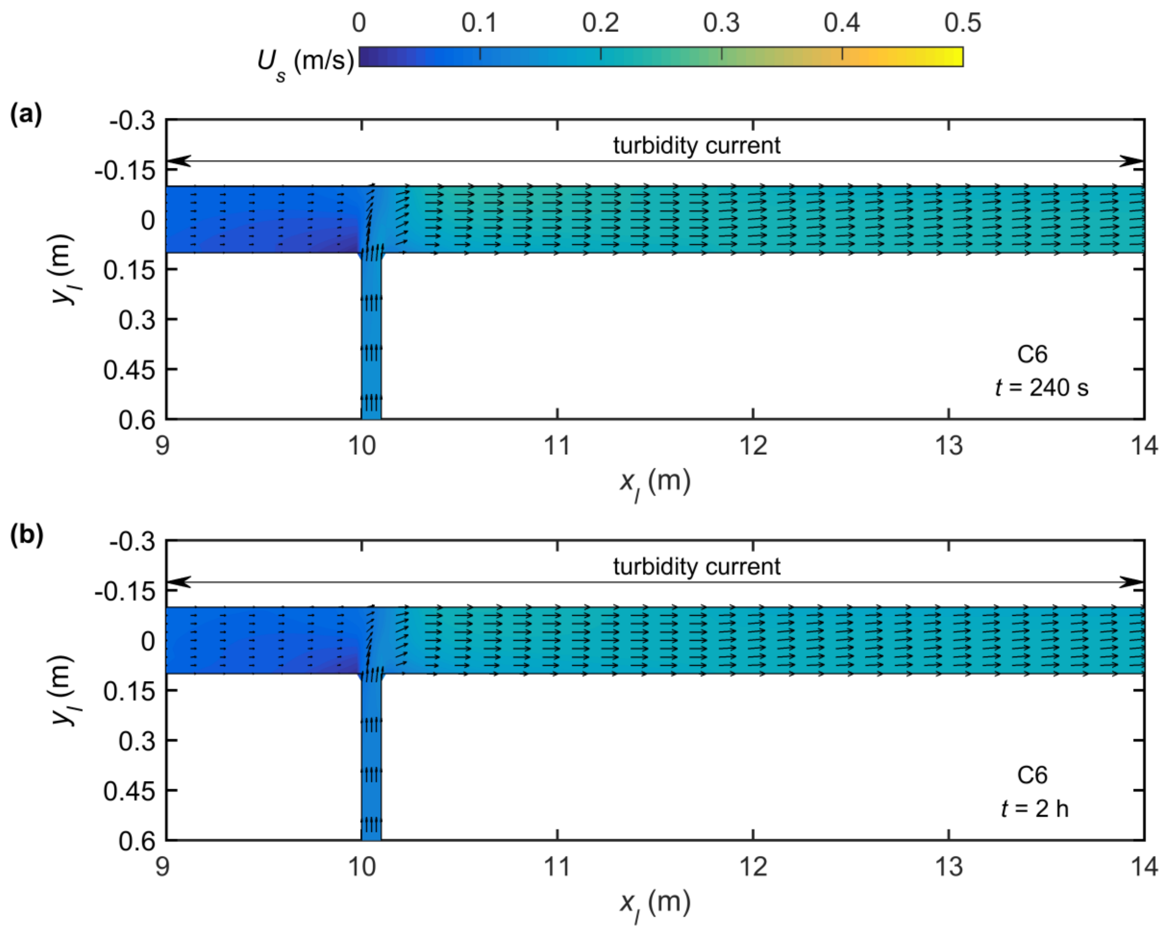

Fig. 10 Velocity field of turbidity current within the confluence for Case C6, at times **(a)**

$t = 240\,\mathrm{s}$, and **(b)** $t = 2\,\mathrm{h}$

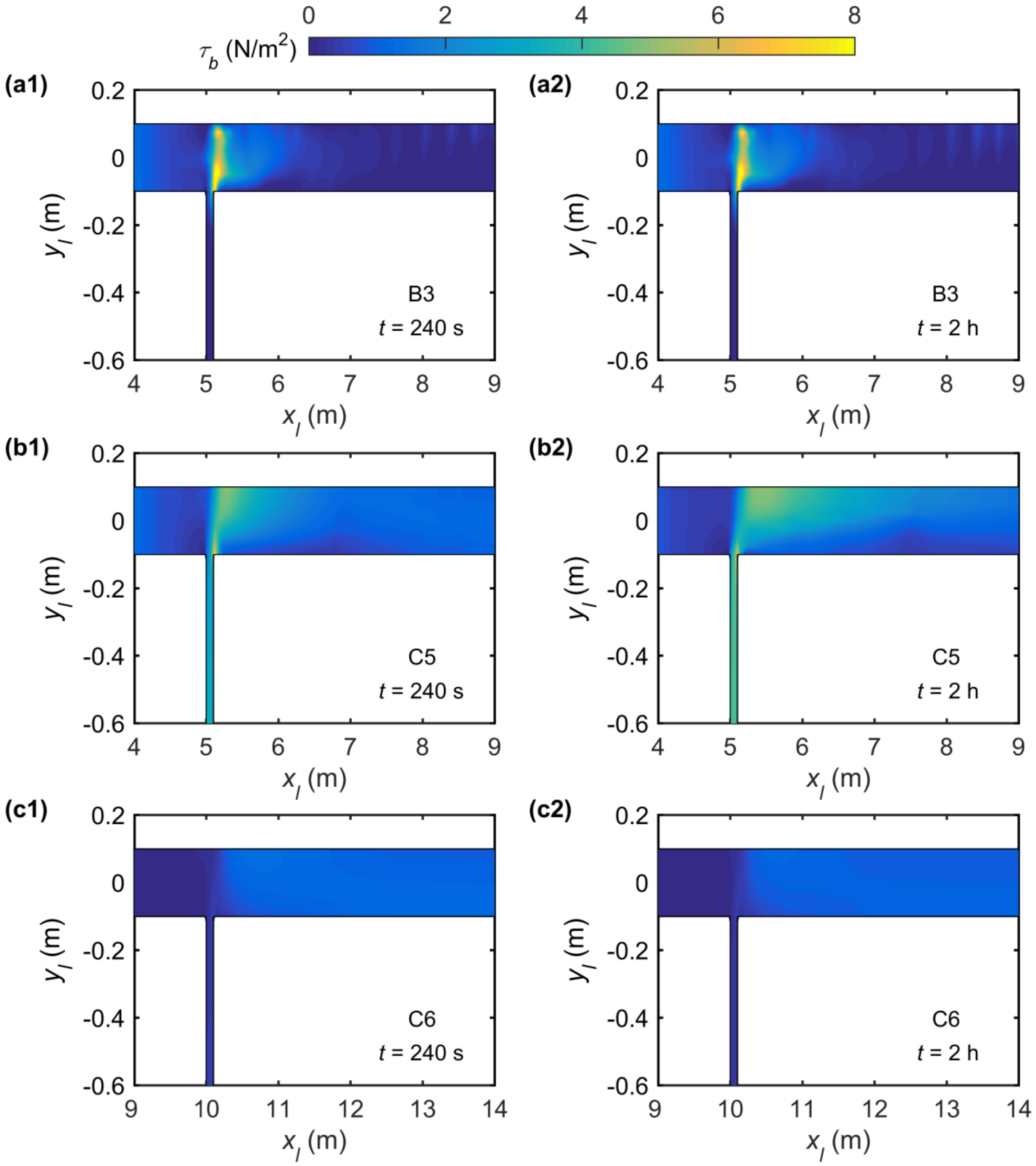

Fig. 11 Planar distributions of bed shear stress τ_b magnitude at confluence at times t = 240 s and t = 2 h for **(a1-a2)** Case B3, **(b1-b2)** Case C5, and **(c1-c2)** Case C6

Significantly, two flow exchange patterns have distinct effects on the velocity field and bed shear stress of the reservoir turbidity current. With the intrusion of reservoir turbidity current from the MC to the TR, a lateral variation of turbidity current velocity occurs at the confluence (Fig. 8), different from Case A1 that experiences changes solely in the longitudinal velocity component (Fig. 7). With the heavily sediment-laden flow plunging from the TR into the turbidity current in the MC, the flow dynamics near the confluence is mainly affected by the junction location. For a junction located upstream of the OSPP, the flow structure of the turbidity current at the confluence resembles the pattern described by Best [40] (Fig 9). By contrast, features of the turbidity current velocity field effectively disappear when the junction is located downstream of the OSPP, due to the increased layer thickness of the turbidity current at the confluence (Figs. 6 and 10). Compared to the case without a TR, the tributary inflow conditions cause the local bed shear stress to increase, which can initiate sediment transport at the junction.

3.5 Sediment transport

The effects of tributary inflow conditions on volumetric sediment concentration, and longitudinal and transverse sediment transport rates per unit channel width are displayed in Figs. 12-15 for Cases A1, B1-B4, and C1-C6.

In general, as the reservoir turbidity current propagates, the sediment concentration c_s reduces longitudinally along the MC in the absence of TR (Fig. 12a1), while the longitudinal sediment transport rate per unit width $h_s u_s c_s$ usually remains below 3.0 cm^2/s (Fig. 12b1), and there is no transverse sediment transport. On being vented through the BSFT, the sediment concentration and sediment transport rate of the reservoir turbidity current exhibit almost no change from t = 240 s to t = 2 h owing to the imposed steady upstream boundary condition (Figs. 12a2 and 12b2). In cases where the TR is present, the situation is quite different. In Cases B1 and B3, as the MC turbidity current intrudes into the junction, sediment concentration in the TR decreases longitudinally, and the lowest sediment concentration occurs at the intrusion front inside the TR (Figs. 13a and 13c). The longitudinal sediment transport rate per unit width increases at the downstream junction corner (Figs. 14a and 14c), while the transverse sediment transport rate per unit width at the central junction is negative, being deflected by the inflow from the TR (Figs. 15a and 15c). Additionally, the MC turbidity current further intrudes into the TR in Cases B2 and B4, for which the junction is located downstream of the OSPP (Figs. 13b and 13d). In Cases C1-C6, as the sediment-laden flow from the TR interacts with the reservoir turbidity current in the MC, the longitudinal sediment transport rate per unit width downstream of the junction is increased relative to Case A1 without a TR (Figs. 14e-14j).

Our results for highly concentrated sediment transport at a confluence are noticeably different from previous studies on river confluences carrying low sediment loads or clear water [40, 46]. The discharge ratio, sediment concentration ratio, and junction location are key factors that control sediment transport near a confluence. For a heavily sediment-laden flow plunging from a TR into a turbidity current in the MC, the highest levels of sediment concentration in the MC occur downstream of the flow deflection zone. As the discharge ratio increases, the TR sediment concentration becomes more uniform (Figs. 13e and 13i, 13f and

13j). When the junction is located upstream of the OSPP, the longitudinal and transverse sediment transport rates per unit width increase in the region of maximum velocity but decrease within the flow separation zone (Figs. 14i and 15i). When the junction is located downstream of the OSPP, the planar distribution of sediment transport rates is no longer evident because of the featureless flow dynamics at the confluence (Figs. 14j and 15j).

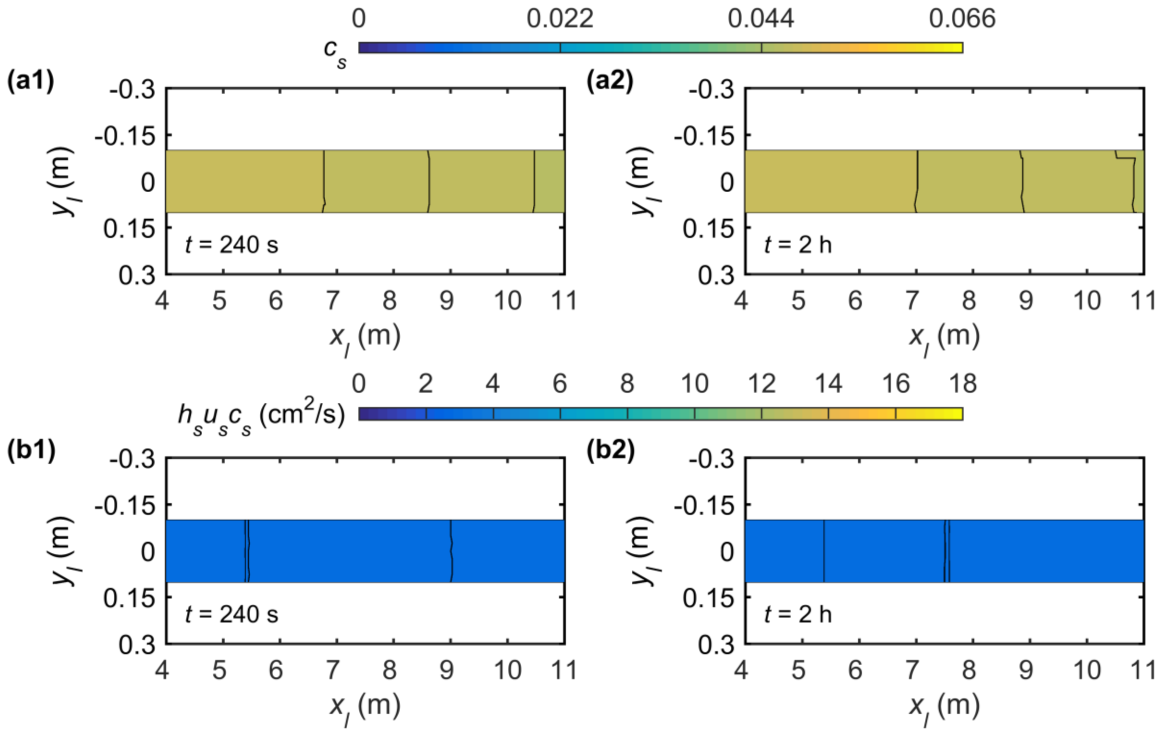

Fig. 12 (a1-a2) Volumetric sediment concentration c_s, **(b1-b2)** longitudinal sediment transport rate per unit width $h_s u_s c_s$ for Case A1 at times t = 240 s and t = 2 h

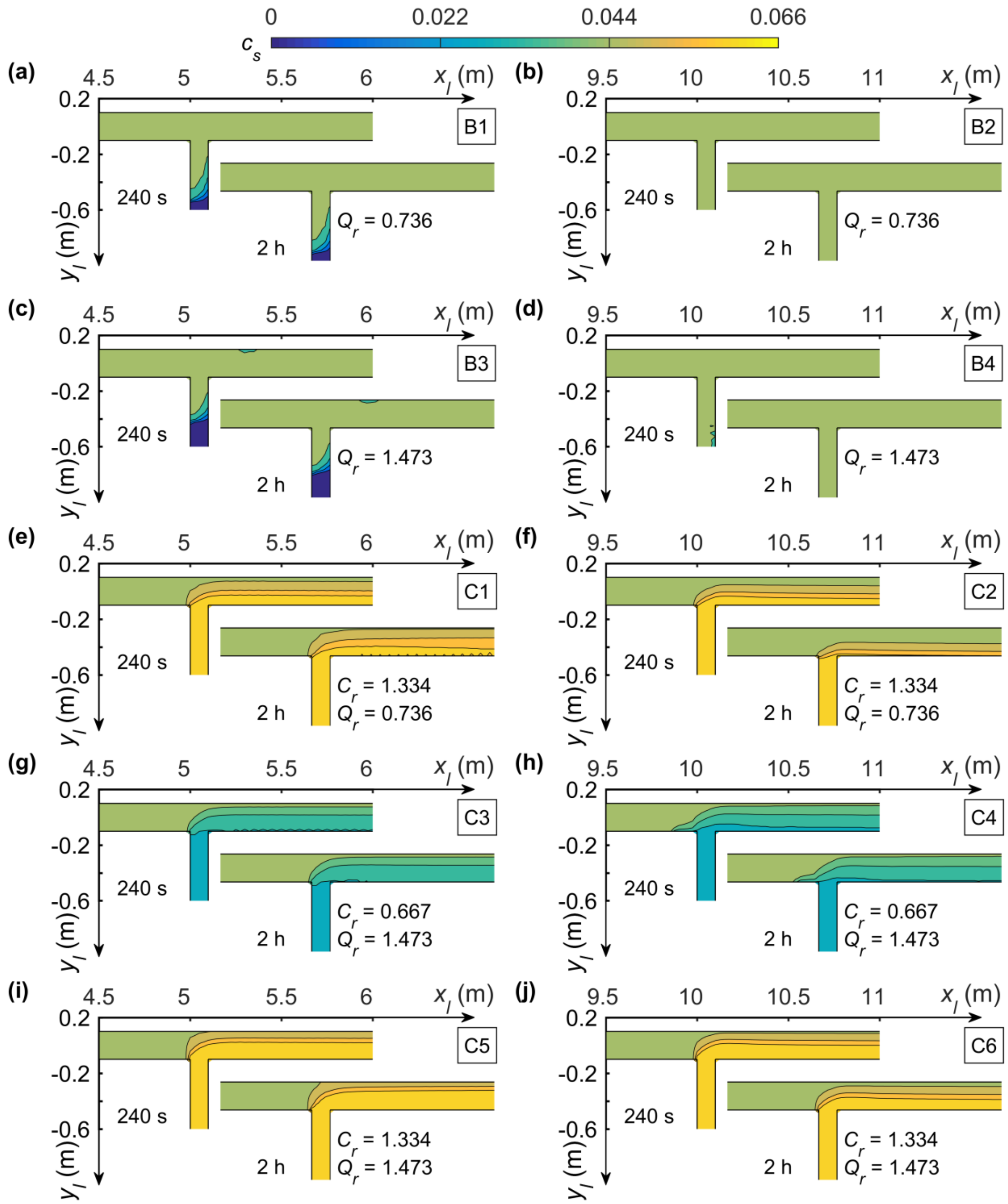

Fig. 13 Volumetric sediment concentration c_s within the confluence at times t = 240 s and t = 2 h for Cases B1-B4, and C1-C6 in **(a) - (j)**

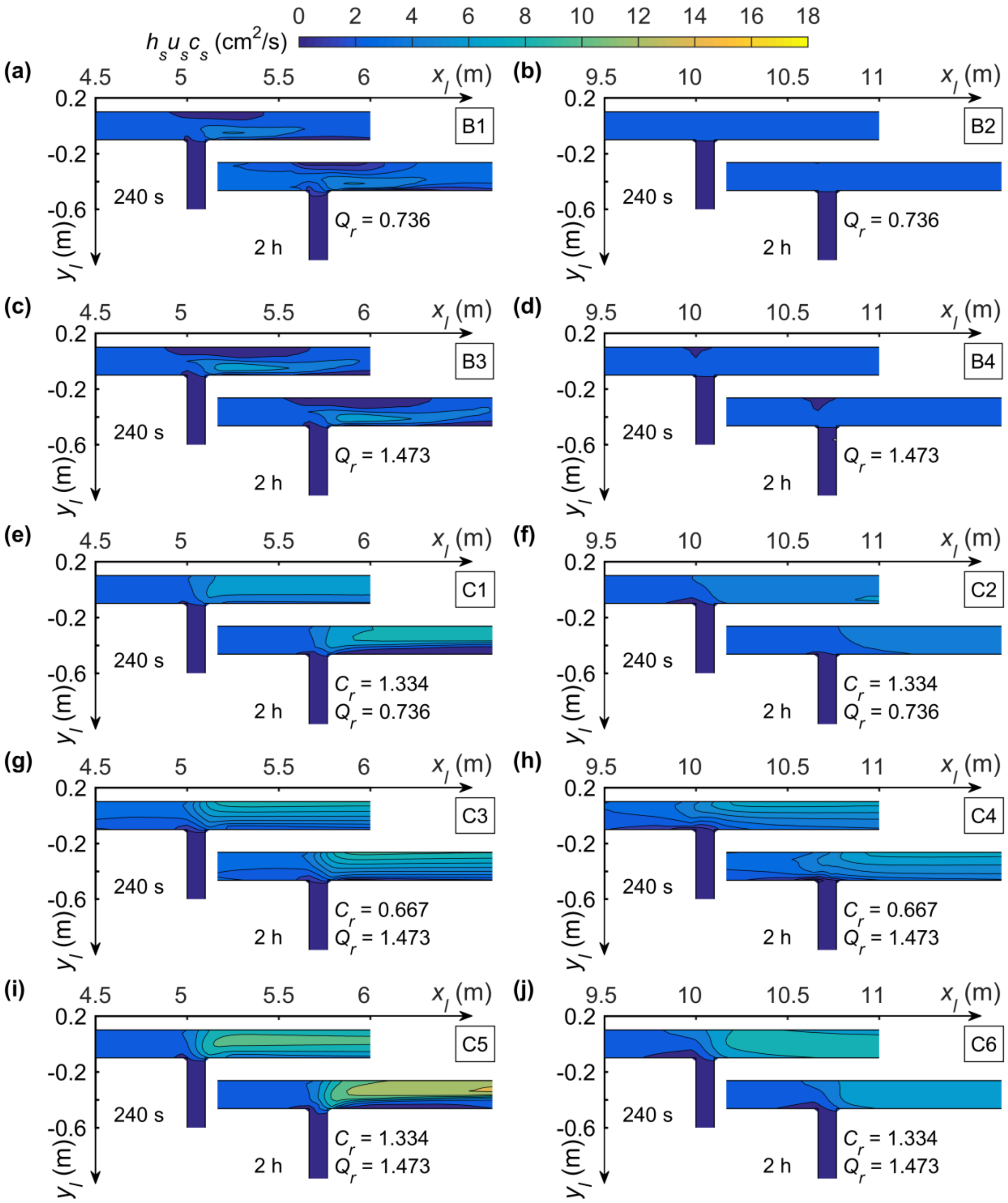

Fig. 14 Longitudinal sediment transport rate per unit width $h_s u_s c_s$ within the confluence at times t = 240 s and t = 2 h for Cases B1-B4, and C1-C6 in **(a) - (j)**

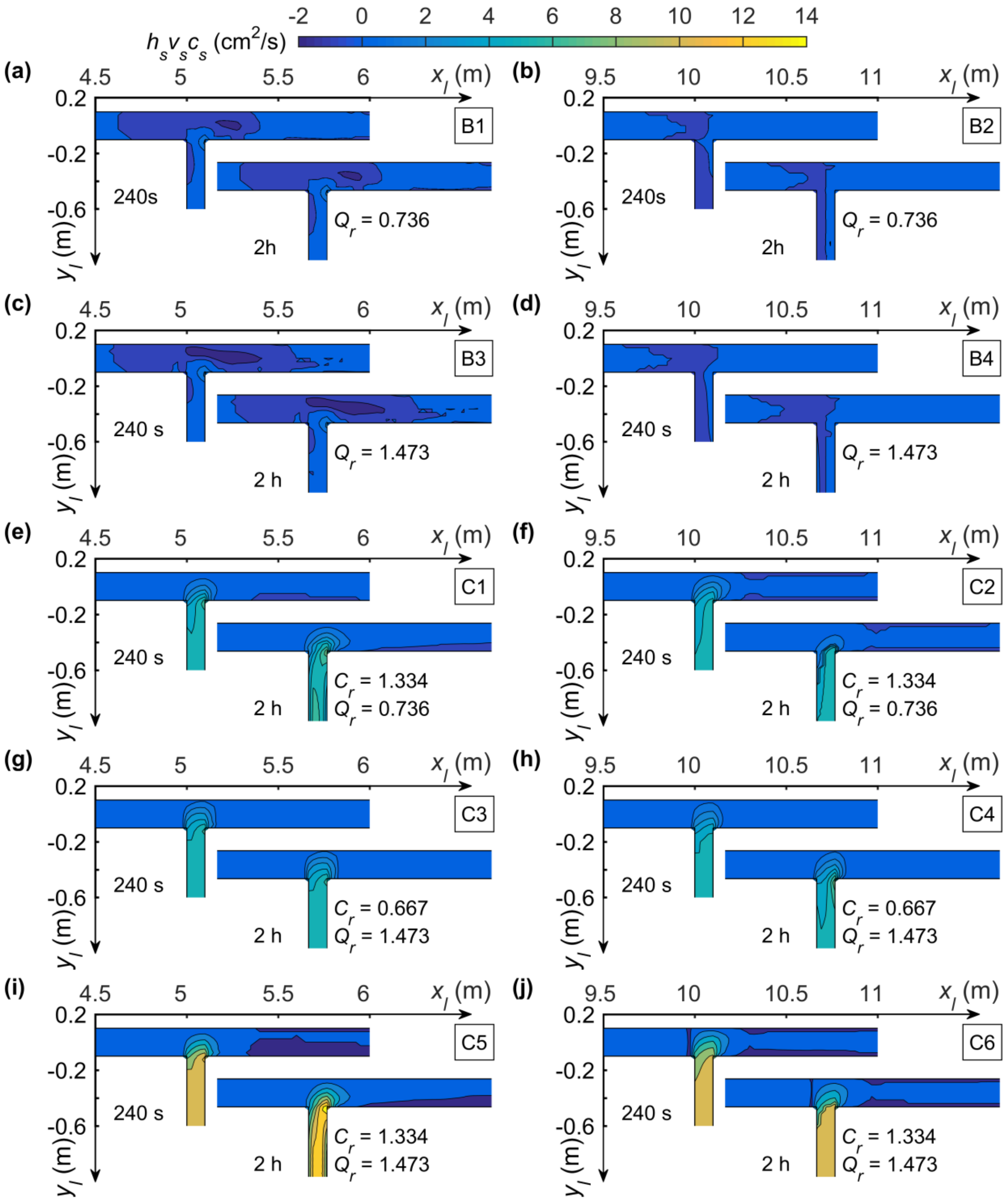

Fig. 15 Transverse sediment transport rate per unit width $h_s v_s c_s$ within the confluence at times t = 240 s and t = 2 h for Cases B1-B4, and C1-C6 in **(a) - (j)**

3.6 Bed deformation

Fig. 16 illustrates the spatial distribution of bed deformation depth, defined as

$\Delta z_b = z_b(x, y, t) - z_b(x, y, 0)$, at time t = 2 h, for Cases A1, B1-B4, and C1-C6. Comparison between the Series B and Series C results in Fig. 16 helps reveal the impacts of junction location, discharge ratio, and sediment concentration ratio on bed morphology at an idealized river confluence.

Bed aggradation occurs upstream of the dam as the turbidity current propagates along the MC (Fig. 16a). Tributary inflow conditions affect local bed deformation at the confluence. Specifically, when the junction is located upstream of the OSPP and $C_r > 1$, as in Cases C1 and C5, the majority of sediment is conveyed downstream through the central junction, with the remainder partly deposited in the flow stagnation and separation zones owing to the reduced flow velocity (Figs. 16f and 16j). A thalweg is created at the TR extending a short distance across the MC by sediment deposition in the flow stagnation zone and separation zone. A separation zone bar extends downstream and towards the opposite side of the MC, resembling bed deformation at a river confluence as described by Zhang et al. [32, 33]. The flow separation zone is influenced by the discharge ratio [47], with a larger separation zone bar occurring for Case C5 compared with that for Case C1 (Figs. 16f and 16j). The location of the junction also has a profound effect on bed deformation. When the junction is located upstream of the OSPP and $C_r < 1$, as in Cases B1, B3 and C3, bed deformation is hardly discernible at the confluence (Figs. 16b, 16d and 16h). When the junction is located downstream of the OSPP, as in Cases C2, C4 and C6, the width of the flow separation zone decreases (Fig. 10), hindering formation of the separation zone bar (Figs. 16g, 16i and 16k). Moreover, as the MC turbidity current intrudes into the junction in Cases B2 and B4, the lower speed of the sediment-laden flow layer in the TR promotes sediment deposition and bed aggradation inside the TR (Figs. 16c and 16e).

Tributary inflow has a significant effect on bed morphology at a river confluence. In particular, the sediment concentration ratio and junction location provide the most important controls on bed deformation. When both the MC and TR carry highly concentrated sediment-laden flows and the junction is located upstream of the OSPP, the bed morphology near the confluence develops a bar in the stagnation zone at the upstream junction corner, a bar in the flow separation zone below the downstream junction corner, and a thalweg for sediment transport through the central junction. These are in contrast with the scour hollow and avalanche faces observed in previous research on river confluences with clear water or low sediment loads [46, 48, 49]. Consequently, tributary inflow and sediment input conditions dominate hydro-sediment-morphodynamic processes at a river confluence.

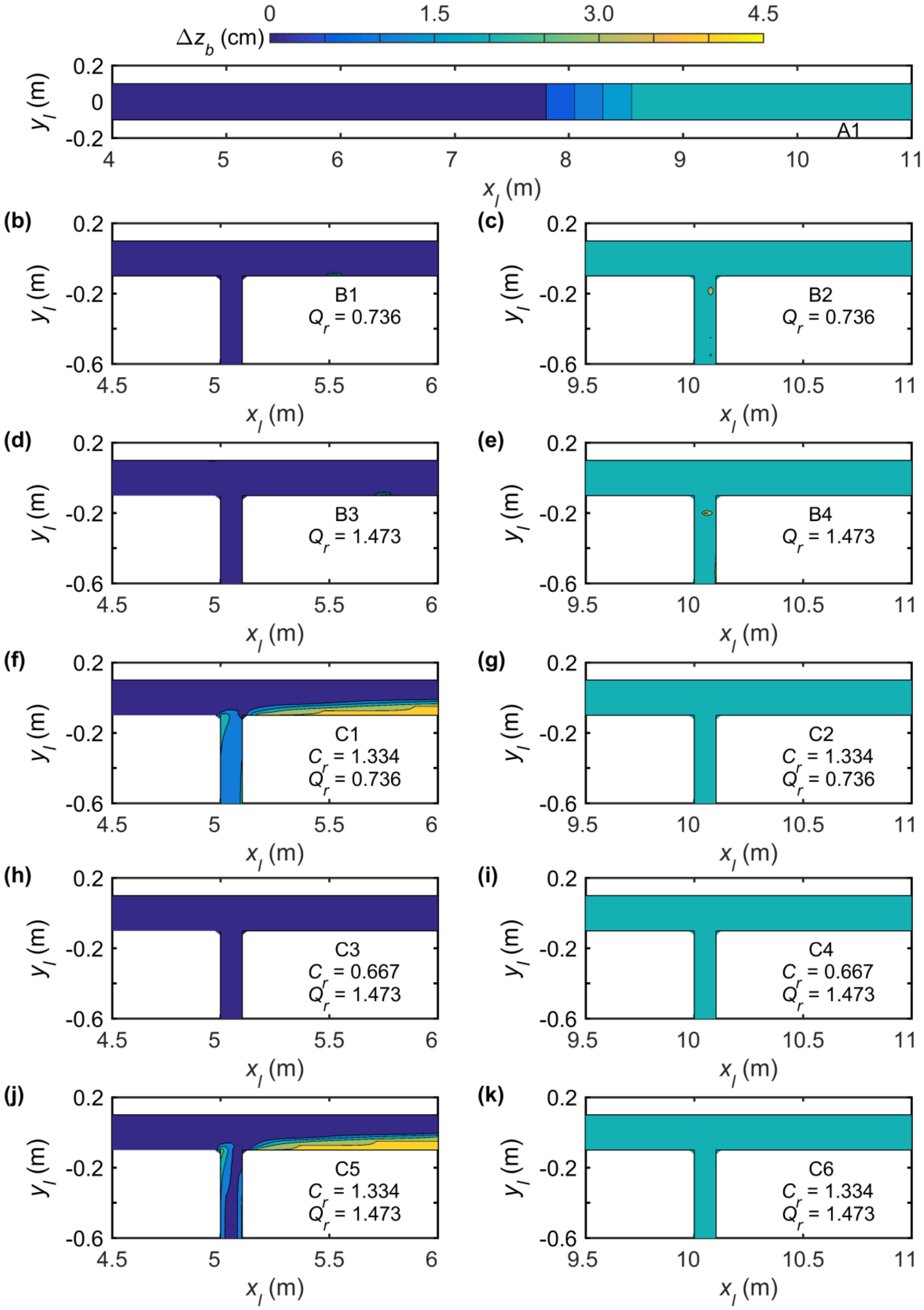

Fig. 16 Spatial distribution of bed deformation depth Δz_b at t = 2 h for Cases A1, B1-B4, and C1-C6 in **(a) - (k)**

3.7 Sediment flushing efficiency

We finally probe into how sediment flushing by a turbidity current is affected by the tributary inflow. Here, sediment flushing efficiency E_{sf} is defined as the ratio of sediment volume (V_{so}) exiting the bottom outlet (driven by the turbidity current) to the total sediment volume (V_{si}) entering from the MC and TR, where V_{si} and V_{so} are calculated from

$$V_{si}(t) = \iint (h_s u_s c_s)_{inlet} dy\, dt \tag{2}$$

$$V_{so}(t) = \iint (h_s u_s c_s)_{outlet} dy\, dt \tag{3}$$

Fig. 17 shows the evolution of sediment flushing efficiency E_{sf} for Cases A1-A2, B1-B6, and C1-C8 (Table 2). In general, sediment flushing initiates once the turbidity current front reaches the bottom outlet. The flushing efficiency grows rapidly with time during the first 20 minutes or so, then more slowing until a peak value is reached roughly at 1 hr, after which the efficiency either decreases slightly (Cases B2, B4, C2 and C6) or keeps constant roughly. As the turbidity current front arrives (Fig. 4), the bottom sluice gate is opened for sediment flushing through the BSFT, allowing sediment to exit the MC. During the first 20 minutes, with increasing outflow discharge and sediment concentration, the sediment exit rate increases, stimulating the flushing efficiency to increase rapidly. Subsequently, the outflow discharge settles to a stable state as the turbidity current evolves upstream of the dam, whilst the sediment output rate exhibits a similar trend. Thus, the flushing efficiency increases slowly until reaching a peak at 1 hr. It should be noted that the sediment output decreases due to severe long-term sediment deposition in cases involving a junction located further downstream, such as Cases B2, B4, C2, C6 and C8 (Fig. 17).

As shown in Fig. 17, sediment flushing efficiency E_{sf} increases with the increase of sediment concentration C_m of the MC, as per Cases A1 and A2. In Cases B1-B6 and C1-C8, the presence of clear-water or highly concentrated sediment-laden flow in the TR lowers the efficiency of sediment flushing as compared against its counterpart without tributary inflow. For cases with clear-water inflow from upstream of the TR, the MC turbidity current is diluted by the tributary inflow and the concurrent intrusion of the MC turbidity current into the TR. Both lead to a reduction in sediment concentration of the MC turbidity current, and so cause the sediment flushing efficiency to fall. For cases with sediment-laden inflow from the TR, more sediment deposits inside the TR and around the confluence, and thus sediment flushing efficiency is considerably lower than the cases with clear-water inflow from the TR. Notably, sediment-laden inflow from the TR with a higher sediment concentration ratio C_r reinforces the MC turbidity current, thereby leading to higher sediment flushing efficiency as found in Cases C3 and C5, C4 and C6.

Briefly, the sediment flushing efficiency pertains to the specific sediment particle size under the flow conditions, and the effect of tributary inflow on sediment flushing efficiency by the turbidity current is so significant that it should be taken into account in reservoir sedimentation management and the maintenance of reservoir capacity.

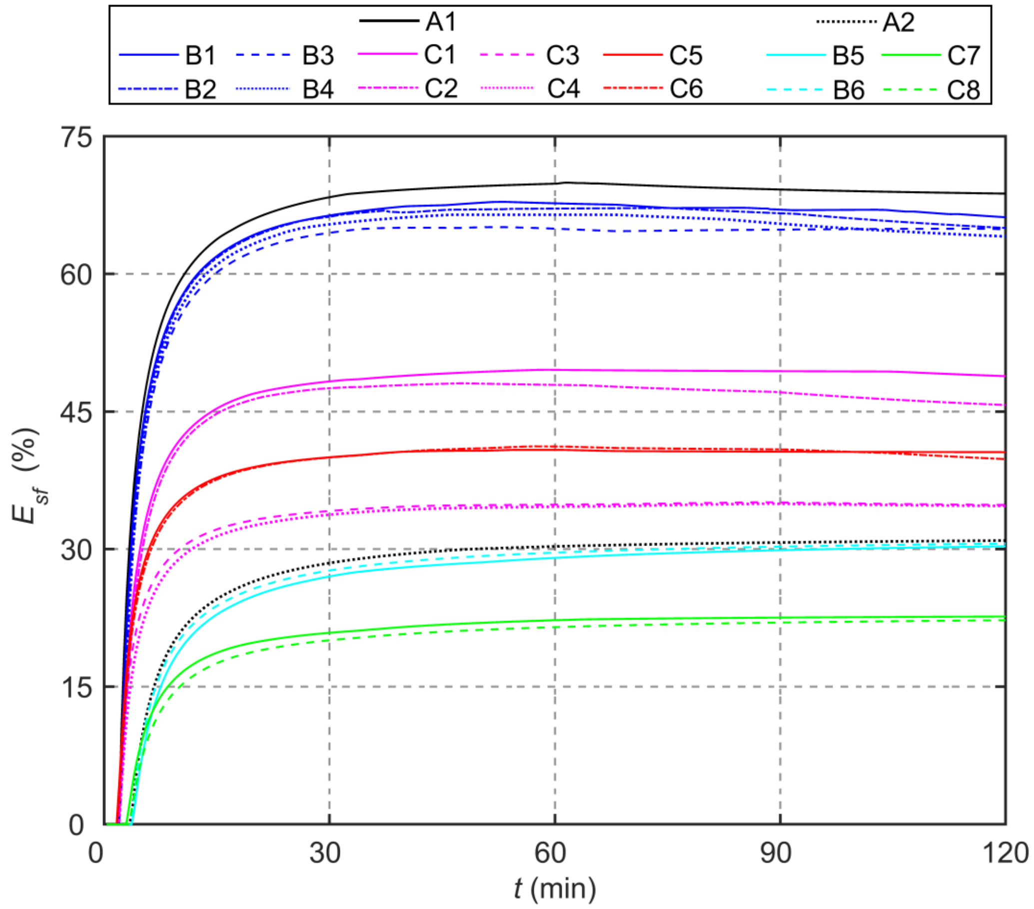

Fig. 17 Time histories of sediment flushing efficiency E_{sf} for different tributary inflow conditions

3.8 Discussion

3.8.1 Effects of tributary configuration

The numerical results presented in sections 3.1, 3.2 and 3.7 demonstrate that tributary inflows have an appreciable effect on the formation and propagation of MC turbidity current and sediment flushing efficiency. Here, the results are further extended for other parameter controls listed in Table 2 (i.e., tributary bed slope i_{bt}, junction angle θ, and width ratio W_r), corresponding to Fig. 18 and Fig. S2 given in the Supporting Information online.

Compared to Case A1 without a TR, the MC turbidity current propagation is slower for cases with clear-water inflow from upstream of the TR. If the junction is located downstream of the OSPP, a larger width ratio W_r, a lower tributary bed slope i_{bt}, or a smaller junction angle θ causes the turbidity current to propagate more slowly, demonstrated by the front location in Cases B4, B8, B10, and B12 (Fig. 18b). However, these controls exert a minor influence in cases where the junction is located upstream of the OSPP (Fig. 18a). This is primarily because the width ratio W_r, tributary bed slope i_{bt}, and junction location together control the intrusion distance of the turbidity current from MC to TR, leading to lower sediment concentration and thus a smaller driving force for the MC turbidity current. Clear-water flow from the TR with discharge ratio $Q_r > 1$ and smaller junction angle $\theta = 45^o$ drives a longitudinal flow of the upper layer in the MC, which increases interface resistance to the turbidity current and slows down the propagation of the turbidity current. The results shown in Figs. 18a and 18b demonstrate that the foregoing controls have a slight influence on the formation of MC turbidity current, corresponding to the location and depth at plunge points along the central line of the MC. However, this role cannot be neglected in cases involving sediment-laden flow from upstream of the TR. Notably, for Cases B7-B12 with clear-water inflows from upstream of TR, the control parameters, W_r and i_{bt} with a larger value slightly lower sediment flushing efficiency. Additionally, clear-water inflow from the TR with smaller junction angle θ causes sediment flushing efficiency to fall, especially when the junction is located upstream (Fig. S2a).

Figs. 18c and 18d indicate that for sediment-laden inflow from the TR, even if the tributary configuration is modified, it is still conducive to the propagation of the MC turbidity current compared with Case A1 without the TR, and has a significant influence on plunge point location. Compared with Case C5, the distance between the plunge point and main flume entrance increases discernibly with increasing width ratio W_r, but decreases with increasing junction angle θ, corresponding to Cases C9 and C13. The influence of tributary bed slope i_{bt} is minor. Notably, there is lateral variation in the plunge point position of Case C13 with $\theta = 45^o$, which is quite distinct from that of Case C5 with $\theta = 90^o$ (see Fig. R3 in the Support Information online). The turbidity current front located further downstream of the MC has a higher tributary bed slope i_{bt} or a smaller junction angle θ, as in Cases C11 and C13, C12 and C14. By contrast, a slower advance of turbidity current front is generally obtained with larger width ratio W_r, corresponding to Cases C9 and C10. Physically, given that the inflow discharge of TR is specified (Table 2), the velocity of sediment-laden flow from upstream of the TR decreases in relation to a larger width ratio W_r. Therefore, due to the later interaction time with the upstream sediment-laden flow entering from the TR, the MC turbidity current propagates slowly (temporarily). For Cases C9-C14 involving heavily sediment-laden inflows from TR, a larger width ratio W_r, or a higher tributary bed slope i_{bt}, or a smaller junction angle θ lowers sediment flushing efficiency compared with Cases C5 and C6 (Fig. S2). Sediment flushing efficiencies rise faster at first in cases with higher tributary bed slope i_{bt} and smaller junction angle θ (i.e., Cases C12 and C14), and then decrease slightly or saturates because of long-term sediment deposition in the MC. A tributary configuration with a larger W_r leads to a reduction in sediment flushing efficiency, especially when the TR is located downstream (Fig. S2b).

Succinctly, although the tributary configuration modifies the interaction between MC and TR, our findings concerning the effect of tributary inflow on reservoir turbidity current, as shown in Figs. 3-17, appear to hold. The presence of a tributary has significant implications for the advance of a turbidity current front and the efficiency of sediment flushing, which must be taken into account in the timely operation of bottom outlets under a dam so that sediment can be thoroughly flushed out of the reservoir.

The present computational study is limited to uniform sediment. It is intended to consider the effect of different sediment size distributions from the MC and TR on reservoir turbidity currents in a future study. Although this study has mainly focused on laboratory-scale cases, prototype-scale cases merit further investigation, such as the Guxian Reservoir, planned for the middle Yellow River, China.

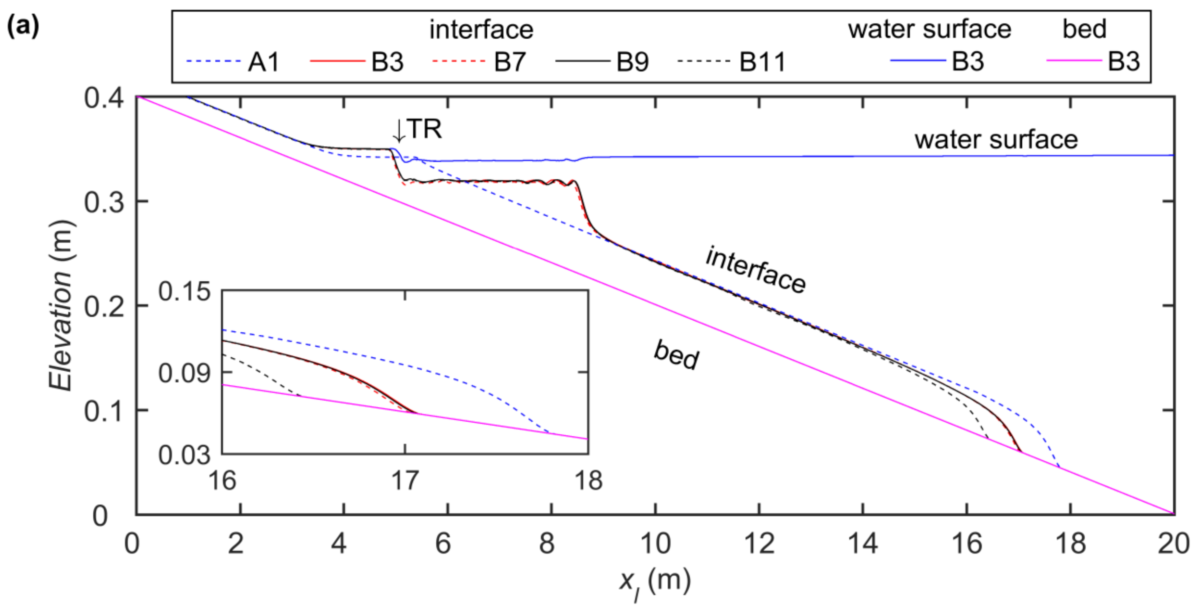

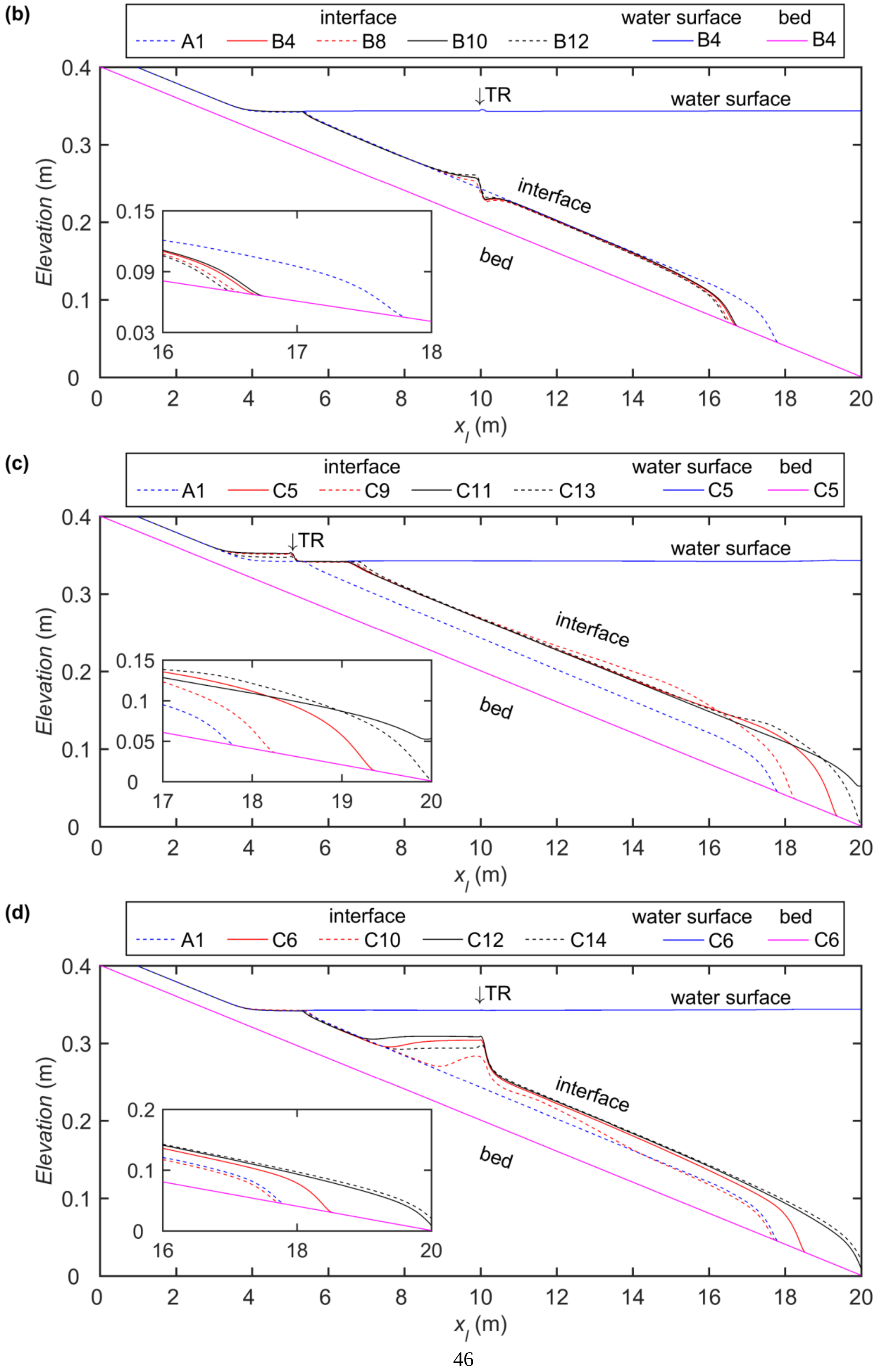
(b)
interface
A1
B4
B8
B10
B12
water surface
B4
bed
B4
↓TR
water surface
interface
bed
Elevation (m)
x_l (m)
(c)
interface
A1
C5
C9
C11
C13
water surface
C5
bed
C5
↓TR
water surface
interface
bed
Elevation (m)
x_l (m)
(d)
interface
A1
C6
C10
C12
C14
water surface
C6
bed
C6
↓TR
water surface
interface
bed
Elevation (m)
x_l (m)

Fig. 18 Water surface, interface and bed profiles along the central line of the MC at $t = 100\,\mathrm{s}$ for Cases: **(a)** A1, B3, B7, B9, and B11; **(b)** A1, B4, B8, B10, and B12; **(c)** A1, C5, C9, C11, and C13; and **(d)** A1, C6, C10, C12, and C14

3.8.2 Dimensional analysis of sediment flushing efficiency

All the foregoing findings are based on numerical modelling of laboratory-scale cases. Although dimensional analysis is unrealistic for the spatial-temporal processes characterizing the effects of tributary inflows on reservoir turbidity currents, we conduct dimensional analysis of the sediment flushing efficiency E_{sf}. To gain more insight into the sediment flushing efficiency E_{sf}, 26 cases (listed in Table 2) and a 22 supplementary cases (summarized in Table S1) are now investigated. Buckingham's π theorem, together with dimensional homogeneity, is applied to derive the non-dimensional variables. Then the stable sediment flushing efficiency (at 1 hr approximately) is plotted as dimensionless graphs through which an exponential relationship is obtained (See Text S1 in the online Support Information for further details). From the results in Supplementary Fig. S4, the best fit curve for the sediment flushing efficiency takes the form:

$$E_{sf1} = \begin{cases} 2.468 Q_r^{-0.024} C_m^{0.406} W_r^{-0.020} i_{br}^{0.001} \theta^{0.023} L_d^{-0.036} & \text{Series B} \\ \\ 0.999 Q_r^{-0.210} C_m^{0.359} C_r^{0.227} W_r^{-0.054} i_{br}^{0.044} \theta^{0.026} L_d^{0.042} & \text{Series C} \end{cases} \qquad (4)$$

Eq. (4) above, in fact, relates the sediment flushing efficiency to the TR-to-MC discharge ratio Q_r, volumetric sediment concentration C_m of MC, the TR-to-MC volumetric sediment concentration ratio C_r, the TR-to-MC width ratio W_r, the TR-to-MC bottom slope ratio i_{br}, junction angle θ, and the dimensionless distance $L_d = L_t / h_0$ from dam to junction. Three conventional metrics are introduced for quantitative evaluation, i.e., the percentage bias (PBIAS) [50], the Nash-Sutcliffe efficiency (NSE) [51], and the coefficient of determination (R^2):

$$\text{PBIAS} = \frac{\sum_{i=1}^{n}\left(E_i^{fit} - E_i^{mod}\right)}{\sum_{i=1}^{n}\left(E_i^{mod}\right)} \tag{5a}$$

$$\text{NSE} = 1 - \frac{\sum_{i=1}^{n}\left(E_i^{fit} - E_i^{mod}\right)^2}{\sum_{i=1}^{n}\left(E_i^{mod} - \bar{E}^{mod}\right)^2} \tag{5b}$$

$$\text{R}^2 = 1 - \frac{\left(\sum_{i=1}^{n}\left(E_i^{mod} - \bar{E}^{mod}\right)\left(E_i^{fit} - \bar{E}^{fit}\right)\right)^2}{\sum_{i=1}^{n}\left(E_i^{mod} - \bar{E}^{mod}\right)^2 \sum_{i=1}^{n}\left(E_i^{fit} - \bar{E}^{fit}\right)^2} \tag{5c}$$

where E_i^{mod} represents the computational model result and $\bar{E}^{mod}$ is its mean value; E_i^{fit} represents the fitted value from Eq. (4) and $\bar{E}^{fit}$ is the fitted mean value. PBIAS illustrates the tendency of the fitted value to be larger or smaller than the computational model counterpart, and a value of zero means the fit is good. Moreover, the closer the values of the metric NSE and R^2 are to 1, the higher is the accuracy of the fitted relationship.

Fig. 19 displays the computational model results for a total of 48 laboratory-scale cases together with the theoretical ones obtained by the conducted dimensional analysis. The corresponding results for sediment flushing efficiency are shown to be in agreement. This is confirmed by the percentage bias (PBIAS = 0.0001), Nash-Suttcliffe efficiency (NSE =

0.9943), and correlation coefficient (R^2 = 0.9943) values.

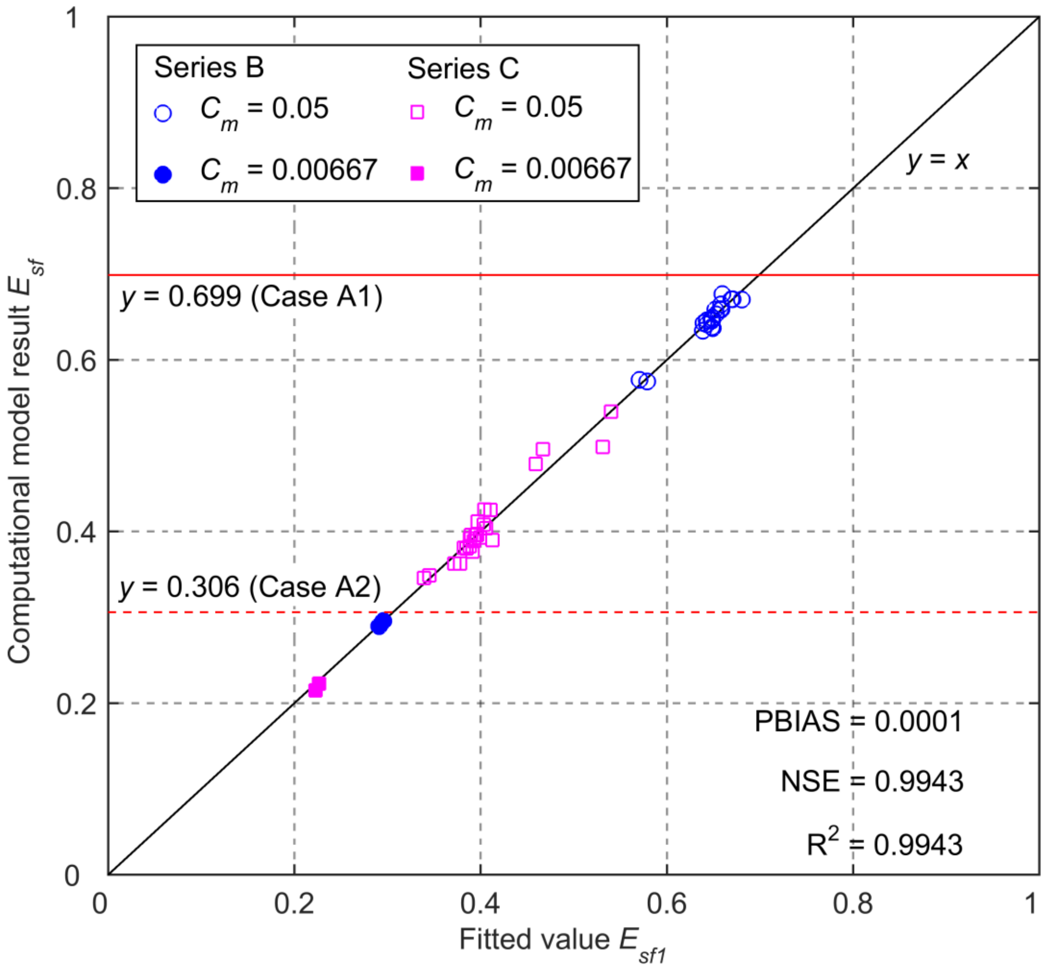

Fig. 19 Computational model results of sediment flushing efficiency compared with fitted values obtained by Eq. (4) for a total of 48 cases

Notably, according to Eq. (4), the sediment flushing efficiency of reservoir turbidity current is mainly controlled by inflow conditions (e.g., sediment concentration C_m of MC) rather than tributary configuration. It is reasonable to drop out the related parameter with weak influence (i.e., bed slope ratio of TR to MC i_{br}), which slightly simplifies Eq. (4) for sediment flushing efficiency, as represented by Eq. (S7) in the Supporting Information online.

It should also be noted that the dimensional analysis of sediment flushing efficiency is conducted for specific ranges of nondimensional parameters, i.e., $Q_r \in [0.368, 1.473]$, $C_r \in [0, 1.334]$, $C_m \in [0.00667, 0.05]$, $W_r \in [0.5, 1.0]$, $i_{br} \in [0.3, 1.0]$, $\theta \in [\pi/4, \pi/2]$, and $L_d \in [29.4, 44.1]$. Certainly, sufficient caution must be taken when applying Eq. (4) beyond the validity ranges.

4 Conclusion

The following conclusions are drawn on the effect of a tributary on reservoir turbidity currents, based on a computational study using a 2D double layer-averaged computational model [12].

Tributary effects on turbidity current formation and propagation in the MC mainly depend on tributary discharge, sediment input, and junction location. Tributary configurations (i.e., distinctive width ratio W_r, tributary bed slope i_{bt}, and junction angle θ) also appreciably modify the advance of turbidity current front. Clear-water flow from the TR may cause the stable plunge point to migrate upstream, reducing its thickness and sediment concentration, leading to a slower front advance than in a counterpart MC without tributary inflow. For cases with clear-water flow from the TR, tributary configurations with larger W_r, lower i_{bt} and smaller θ lead to slower propagation of the turbidity current. Sediment-laden inflow from the TR may cause the stable plunge points to migrate downstream, increasing the discharge, thickness and sediment concentration of the reservoir turbidity current, which is also conducive to propagation of the turbidity current. For cases with highly concentrated sediment-laden flow from the TR, tributary configurations with smaller W_r, higher i_{bt}, and smaller θ of lead to faster propagation of the turbidity current.

Compared to its counterpart without tributary inflow, clear-water flow and sediment-laden flow from the TR lower the sediment flushing efficiency as a result of diluting turbidity current and sediment deposition around the confluence. Based on the computational model results and dimensional analysis, sediment concentration is the primary control of sediment flushing efficiency. Notably, for cases with highly concentrated sediment-laden flow from the TR, a higher sediment concentration ratio leads to higher sediment flushing efficiency by reinforcing the MC turbidity current. By contrast, a higher discharge ratio lowers sediment flushing efficiency by diluting the turbidity current.

Tributary location and inflow conditions lead to complicated flow dynamics and bed deformation at the confluence. The velocity field and spatial distribution of bed shear stress of the reservoir turbidity current resemble their counterparts in a confluence flow with a low sediment load or clear water. Yet, the sediment transport and bed deformation of a confluence flow with high sediment concentrations are quite different from those at an ordinary sediment-laden flow confluence. The discharge ratio and sediment concentration ratio are key factors that control bed morphology close to the confluence. When the junction is located upstream of the OSPP, the bed morphology of confluence flows with high sediment concentrations is divided into a bar in the flow stagnation zone, a thalweg for sediment transport through the central junction, and a bar in the flow separation zone, unlike the scour hollow and avalanche faces that develop in river confluences with low sediment loads or clear water.

The present findings indicate that it is important to account for tributary inflow with high sediment load when analysing reservoir turbidity currents. The presence of tributary inflow has significant implications for the formation and evolution of a reservoir turbidity current, and hence the sediment management of reservoirs located along heavily sediment-laden rivers. Nevertheless, further laboratory and field observations are needed to enhance the understanding of bed morphology at a river confluence carrying high sediment loads, especially when the sediment is non-uniform.

Acknowledgments

Information deleted for blind review.

References

1. Wang GQ, Xia JQ, Zhang HW (2002) Theory and practice of hyperconcentrated sediment-laden flow in China. Advances in Hydraulics and Water Engineering - 13th IAHR-APD Congress, Singapore.
2. Wang ZY, Qi P, Melching CS (2009) Fluvial hydraulics of hyperconcentrated floods in Chinese rivers. Earth Surface Processes and Landforms 7(34): 981-993. https://doi.org/10.1002/esp.1789
3. Wan ZH, Wang ZY (1994) Hyperconcentrated flow. IAHR monograph series. Balkema, Rotterdam, The Netherlands
4. Clerici A, Perego S (2000) Simulation of the Parma River blockage by the Corniglio landslide (Northern Italy). Geomorphology 33(1): 1-23. https://doi.org/10.1016/S0169-555X(99)00095-1

5. Cao ZX, Pender G, Carling P (2006) Shallow water hydrodynamic models for hyperconcentrated sediment-laden floods over erodible bed. Advances in Water Resources 29(4): 546-557. https://doi.org/10.1016/j.advwatres.2005.06.011
6. Li W, Su Z, van Maren DS, Wang Z, de Vriend HJ (2017) Mechanisms of hyperconcentrated flood propagation in a dynamic channel-floodplain system. Advances in Water Resources 107: 470-489. https://doi.org/10.1016/j.advwatres.2017.05.012
7. Li W, van Maren DS, Wang ZB, de Vriend HJ, Wu B (2014) Peak discharge increase in hyperconcentrated floods. Advances in Water Resources 67(4): 65-77. https://doi.org/10.1016/j.advwatres.2014.02.007
8. Li W, Xie GH, Hu P, He ZG, Wang YJ (2019) Mechanisms of peak discharge increase in the Yellow River floods and its influencing factors. Journal of Hydraulic Engineering 50(9): 1111-1122 (in Chinese). https://doi.org/10.13243/j.cnki.slxb.20190103
9. Best J (2019) Anthropogenic stresses on the world's big rivers. Nature Geoscience 12(1): 7-21. https://doi.org/10.1038/s41561-018-0262-x
10. Armanini A (2013) Granular flows driven by gravity. Journal of Hydraulic Research 51(2): 111-120. https://doi.org/10.1080/00221686.2013.788080
11. Cantero Chinchilla FN, Dey S, Castro Orgaz O, Ali SZ (2015) Hydrodynamic analysis of fully developed turbidity currents over plane beds based on self-preserving velocity and concentration distributions. Journal of Geophysical Research: Earth Surface 120(10): 2176-2199. https://doi.org/10.1002/2015JF003685
12. Cao ZX, Li J, Pender G, Liu QQ (2015) Whole-process modeling of reservoir turbidity currents by a double layer-averaged model. Journal of Hydraulic Engineering 141(2): 04014069. https://doi.org/10.1061/(ASCE)HY.1943-7900.0000951
13. Chamoun S, De Cesare G, Schleiss AJ (2016) Managing reservoir sedimentation by venting turbidity currents: A review. International Journal of Sediment Research 31(3):

195-204. https://doi.org/https://doi.org/10.1016/j.ijsrc.2016.06.001

14. Ford DE, Johnson MC (1983) An assessment of reservoir density currents and inflow processes. Ford Thornton Norton and Associates LTD, Vicksburs Ms

15. Hu P, Cao ZX, Pender G, Tan GM (2012) Numerical modelling of turbidity currents in the Xiaolangdi reservoir, Yellow River, China. Journal of Hydrology 464: 41-53. https://doi.org/10.1016/j.jhydrol.2012.06.032

16. Wang Z, Xia J, Li T, Deng S, Zhang J (2016) An integrated model coupling open-channel flow, turbidity current and flow exchanges between main river and tributaries in Xiaolangdi Reservoir, China. Journal of Hydrology 543: 548-561. https://doi.org/10.1016/j.jhydrol.2016.10.023

17. Xia CC (2019) Coupled mathematical modelling of shallow water flow and substance transport in open channels (in Chinese). Wuhan University, Wuhan, China

18. Georgoulas AN, Angelidis PB, Panagiotidis TG, Kotsovinos NE (2010) 3D numerical modelling of turbidity currents. Environmental Fluid Mechanics 10(6): 603-635. https://doi.org/10.1007/s10652-010-9182-z

19. An S, Julien PY (2014) Three-dimensional modeling of turbid density currents in Imha Reservoir, South Korea. Journal of Hydraulic Engineering 140(5): 05014004. https://doi.org/10.1061/(ASCE)HY.1943-7900.0000851

20. Lai YG, Huang J, Wu K (2015) Reservoir turbidity current modeling with a two-dimensional layer-averaged model. Journal of Hydraulic Engineering 141(12): 04015029. https://doi.org/10.1061/(ASCE)HY.1943-7900.0001041

21. Wang Z, Xia J, Zhang J, Li T (2018) Modeling turbidity currents in the Xiaolangdi Reservoir with the effect of flow exchanges with tributaries. Advanced Engineering Sciences 50(01): 85-93 (in Chinese). https://doi.org/10.11660/slfdxb.20171205

22. Dai A, Garcia M (2009) Analysis of plunging phenomena. Journal of Hydraulic Research

47(5): 638-642. https://doi.org/10.3826/jhr.2009.3498

23. Li Y, Zhang J, Ma H (2011) Analytical Froude number solution for reservoir density inflows. Journal of Hydraulic Research 49(5): 693-696. https://doi.org/10.1080/00221686.2011.593905

24. Lee HY, Yu WS (1997) Experimental study of reservoir turbidity current. Journal of Hydraulic Engineering 123(6): 520-528. https://doi.org/10.1061/(ASCE)0733-9429(1997)123:6(520)

25. Li J, Cao ZX, Liu QQ (2019) Waves and sediment transport due to granular landslides impacting reservoirs. Water Resources Research 55(1): 495-518. https://doi.org/10.1029/2018WR023191

26. Li J, Cao ZX, Cui Y, Borthwick A (2020) Barrier lake formation due to landslide impacting a river: A numerical study using a double layer-averaged two-phase flow model. Applied Mathematical Modelling 80: 574-601. https://doi.org/10.1016/j.apm.2019.11.031

27. Li J, Cao ZX, Cui Y, Fan X, Yang WJ, Huang W, Borthwick A (2021) Hydro-sediment-morphodynamic processes of the Baige landslide-induced barrier Lake, Jinsha River, China. Journal of Hydrology 596: 126134. https://doi.org/10.1016/j.jhydrol.2021.126134

28. Xiong ZW, Xia JQ, Wang ZH, Li T, Zhang JH (2019) Whole-processes modeling of flow movement and sediment transport during the period of water-sediment regulation in Xiaolangdi Reservoir. Scientia Sinica (Technologica) 49(4): 419-432 (in Chinese). https://doi.org/10.1360/N092017-00295

29. Zhang T, Feng MQ, Chen KL (2020) Hydrodynamic characteristics and channel morphodynamics at a large asymmetrical confluence with a high sediment-load main channel. Geomorphology 356: 107066. https://doi.org/10.1016/j.geomorph.2020.107066

30. Dou ST, Yu X, Zhang JH, Xie WM, Wang WZ, Du XK (2020) Process-based modelling of tributary mouth sandbar evolution in a high sediment-load reservoir. River Research and Applications 36(2): 199-210. https://doi.org/10.1002/rra.3579

31. Han QW (2003) Reservoir deposition (in Chinese). Science Press. Beijing, China

32. Zhang YF, Wang P, Wu BS, Hou SZ (2015) An experimental study of fluvial processes at asymmetrical river confluences with hyperconcentrated tributary flows. Geomorphology 230: 26-36. https://doi.org/10.1016/j.geomorph.2014.11.001

33. Zhang YF, Wang P (2017) Deposition pattern and morphological process at hyperconcentrated flow confluences in upper Yellow River. Journal of Hydroelectric Engineering 36(12): 39-48 (in Chinese). https://doi.org/10.11660/slfdxb.20171205

34. Bonnecaze RT, Hallworth MA, Huppert HE, Lister JR (1995) Axisymmetric particle-driven gravity currents. Journal of Fluid Mechanics 294: 93-121. https://doi.org/10.1017/S0022112095002825

35. Parker G, Fukushima Y, Pantin HM (1986) Self-accelerating turbidity currents. Journal of Fluid Mechanics 171(3): 145-181. https://doi.org/https://doi.org/10.1017/S0022112086001404

36. Zhang RJ, Xie JH (1993) Sedimentation research in China: Systematic selections (in Chinese). China and Power Press. Beijing, China

37. Taylor EH (1944) Flow characteristics at rectangular open-channel junctions. Transactions of the American Society of Civil Engineers 109(1): 893-902. https://doi.org/10.1061/TACEAT.0005772

38. Webber NB, Greated CA (1966) An investigation of flow behaviour at the junction of rectangular channels. Proceedings of the Institution of Civil Engineers 34(3): 321-334. https://doi.org/10.1680/iicep.1966.8925

39. Best JL, Reid I (1984) Separation zone at open-channel junctions. Journal of Hydraulic Engineering 110(11): 1588-1594. https://doi.org/10.1061/(ASCE)0733-9429(1984)110:11(1588)

40. Best JL (1987) Flow dynamics at river channel confluences: implications for sediment transport and bed morphology. Recent Developments in Fluvial Sedimentology 39(5): 27-35. https://doi.org/10.2110/pec.87.39.0027

41. Sukhodolov AN, Rhoads BL (2001) Field investigation of three-dimensional flow structure at stream confluences: 2. Turbulence. Water Resources Research 37(9): 2411-2424. https://doi.org/10.1029/2001WR000317

42. Bradbrook KF, Lane SN, Richards KS, Biron PM, Roy AG (2001) Role of bed discordance at asymmetrical river confluences. Journal of Hydraulic Engineering 127(5): 351-368. https://doi.org/10.1061/(ASCE)0733-9429(2001)127:5(351)

43. Ribeiro ML, Blanckaert K, Roy AG, Schleiss AJ (2012) Flow and sediment dynamics in channel confluences. Journal of Geophysical Research 117(F1): F01035. https://doi.org/10.1029/2011JF002171

44. Lyubimova T, Lepikhin A, Konovalov V, Parshakova Y, Tiunov A (2014) Formation of the density currents in the zone of confluence of two rivers. Journal of Hydrology 508(1): 328-342. https://doi.org/10.1016/j.jhydrol.2013.10.041

45. Ismail H, Viparelli E, Imran J (2016) Confluence of density currents over an erodible bed. Journal of Geophysical Research: Earth Surface 121(7): 1251-1272. https://doi.org/10.1002/2015JF003768

46. Best JL (1988) Sediment transport and bed morphology at river channel confluences. Sedimentology 35(3): 481-498. https://doi.org/10.1111/j.1365-3091.1988.tb00999.x

47. Shaheed R, Yan X, Mohammadian A (2021) Review and comparison of numerical simulations of secondary flow in river confluences. Water 13(14): 1917.

https://doi.org/10.3390/w13141917

48. Herrero H, Díaz Lozada JM, García CM, Szupiany R, Best J, Pagot M (2017) The influence of tributary flow density differences on the hydrodynamic behavior of a confluent meander bend and implications for flow mixing. Geomorphology 304: 99-112. https://doi.org/10.1016/j.geomorph.2017.12.025

49. Sambrook Smith GH, Nicholas AP, Best JL, Bull JM, Dixon SJ, Goodbred S, Sarker MH, Vardy ME (2019) The sedimentology of river confluences. Sedimentology 66(2): 391-407. https://doi.org/10.1111/sed.12504

50. Gupta HV, Sorooshian S, Yapo PO (1999) Status of automatic calibration for hydrologic models: Comparison with multilevel expert calibration. Journal of Hydrologic Engineering 4(2): 135-143. https://doi.org/10.1061/(ASCE)1084-0699(1999)4:2(135)

51. Nash JE, Sutcliffe JV (1970) River flow forecasting through conceptual models part I — A discussion of principles. Journal of Hydrology 10(3): 282-290. https://doi.org/https://doi.org/10.1016/0022-1694(70)90255-6